Research Square

Preprints are preliminary reports that have not undergone peer review.
They should not be considered conclusive, used to inform clinical practice,
or referenced by the media as validated information.

Metabolite-mediated communication reshapes macrophages in hepatocellular carcinoma: single-cell and bulk evidence

Jianfei Shi
The Fourth Hospital of Hebei Medical University
Hua Zhang
The Fourth Hospital of Hebei Medical University
Xin Han
The Fourth Hospital of Hebei Medical University
Jinfeng Wang
The Fourth Hospital of Hebei Medical University
Fei Yin
47100214@hebmu.edu.cn
The Fourth Hospital of Hebei Medical University

Article

Keywords: Hepatocellular carcinoma, MEBOCOST, Metabolite, Macrophages

Posted Date: November 6th, 2026

DOI: https://doi.org/10.21203/rs.3.rs-11321170/v1

License: This work is licensed under a Creative Commons Attribution 4.0 International License.
Read Full License

Additional Declarations:
No competing interests reported.

Tables 1 and 2 are available in the Supplementary Files section.

FRONT MATTER

Title

Metabolite-mediated communication reshapes macrophages in hepatocellular carcinoma: single-cell and bulk evidence

Short title: mCCC reprograms HCC macrophages

Authors

Jianfei Shi[1], Hua Zhang[2], Xin Han[1], Jinfeng Wang[1], Fei Yin[1*]

Affiliations

[1]Department of Gastroenterology and Hepatology, The Fourth Hospital of Hebei Medical University, Shijiazhuang 050019, Hebei, P. R. China;

[2]Department of Infectious Diseases, The Fourth Hospital of Hebei Medical University, Shijiazhuang 050019, Hebei, P. R. China

*Address correspondence to: Fei Yin, Department of Gastroenterology and Hepatology, The Fourth Hospital of Hebei Medical University, Shijiazhuang 050019, Hebei, P. R. China; Email: 47100214@hebmu.edu.cn

Author information

Abstract

Background: This study characterized metabolite-mediated cell-cell communication (mCCC) in the hepatocellular carcinoma (HCC) tumor microenvironment and identified genes with potential therapeutic relevance. Methods: Single-cell and bulk RNA sequencing datasets were analyzed. MEBOCOST was used to infer mCCC networks, followed by high-dimensional weighted gene co-expression network analysis in the main receiver cell type. Candidate genes were obtained by intersecting receiver-related module genes with upregulated differentially expressed genes, then refined using five machine-learning algorithms and cross-cohort validation. Functional analyses included gene set enrichment analysis, immune infiltration profiling, pseudotime analysis, molecular docking, and 100 ns molecular dynamics simulations. Results: Macrophages were identified as the predominant mCCC receiver population, with iron, farnesyl pyrophosphate, and L-glutamine among the prominent signaling metabolites. A co-expression module of 666 genes most strongly correlated with macrophages was identified, and intersection with upregulated DEGs yielded 22 candidate genes. Cross-cohort validation narrowed the machine learning consensus to SNX27 and PEA15 as key genes. Both were negatively enriched in fatty acid metabolism and functionally linked to apoptotic signaling components. Their expression was inversely correlated with infiltration of multiple immune cell populations. SNX27 expression was progressively upregulated along the macrophage differentiation trajectory. Trabectedin exhibited favorable binding affinities for SNX27 (−10.2 kcal/mol) and PEA15 (−9.7 kcal/mol), and both complexes maintained stable conformations over 100 ns MD simulations. Conclusion: These findings suggest that SNX27 and PEA15 may link metabolite-mediated signaling to macrophage-associated remodeling in HCC, and provided preliminary bioinformatic support for further experimental investigation.

Keywords: Hepatocellular carcinoma, MEBOCOST, Metabolite, Macrophages.

MAIN TEXT

Introduction

Hepatocellular carcinoma (HCC) is the most common primary malignant tumor of the liver, with a high mortality rate [1]. Most patients with HCC are diagnosed at intermediate or advanced stages. Combined targeted immunotherapies, such as atezolizumab plus bevacizumab and durvalumab plus tremelimumab, are commonly used treatment options. However, the overall objective response rate remains modest, and drug resistance remains a critical concern[2,3]. Therefore, elucidating the pathogenesis of HCC in depth and exploring novel therapeutic targets remain critical research priorities in this field.

The tumor microenvironment (TME) plays a pivotal role in the progression of HCC and treatment resistance. The TME of HCC is composed of multiple components such as cancer-associated fibroblasts, tumor-associated macrophages, infiltrating immune cells and extracellular matrix proteins, cytokines, and angiogenic mediators. These components collectively promote immune evasion, stromal remodeling, and neovascularization, thereby driving tumor invasion and therapeutic resistance[4]. Chronic inflammation, immunosuppression, and abnormal vascularization within the TME collectively restrict the efficacy of immunotherapy, and the state of the TME is an important factor affecting the treatment response of patients[5.] Metabolic reprogramming is a core feature of HCC. Tumor cells adapt to the severe TME and evade immune surveillance by reshaping pathways such as glycolysis, the pentose phosphate pathway, amino acid metabolism, and fatty acid metabolism. These pathways exhibit complex interactions, with a particularly prominent correlation between acetyl-CoA metabolism and redox homeostasis[6,7.] The Warburg effect, centered on exceptionally enhanced glycolysis, is particularly prominent in HCC. It not only provides energy and synthetic raw materials for the rapid proliferation of tumor cells but also supports tumor growth and invasion by regulating the pH and redox environment of the TME[8]. Metabolites themselves can also act as intercellular signaling molecules, regulating gene expression, cell differentiation and immune response. In the TME, abnormal accumulation or depletion of metabolites might reshape the functional state of immune cells, thereby affecting the anti-tumor immune response. Intercellular communication is the core mechanism for maintaining tissue homeostasis and coordinating tumor progression. Previous studies have mostly focused on ligand-receptor-mediated signal transduction and extracellular vesicles (EVs). Among them, EVs can carry various biomolecules such as DNA, RNA, proteins and metabolites, and participate in regulating the proliferation, invasion, metastasis and chemotherapy resistance of HCC[9]. Metabolite-mediated cell-cell communication (mCCC) has gradually attracted attention in recent years. Metabolites can transmit functional signals by binding to specific receptors or enzymes on target cells and are a crucial component of TME signaling interactions. However, mCCC has long lacked effective quantitative analytical tools; the Metabolite-mediated cell-cell communication scoring tool (MEBOCOST), based on single-cell RNA sequencing (scRNA-seq) and metabolic flux balance analysis, could systematically identify the metabolite signal transduction relationship between donor-recipient cell pairs, which has demonstrated robust performance through multidimensional benchmarking[10.]

In this study, we integrated public bulk and single-cell transcriptome data and systematically analyzed the mCCC network in HCC by using the MEBOCOST tool. mCCC-related candidate genes were identified by combining high-dimensional weighted gene co-expression network analysis (hdWGCNA) and differential expression analysis. Through cross-validation of multiple machine learning algorithms, key genes were further identified. Furthermore, by integrating functional enrichment analysis, immune microenvironment assessment and single-cell trajectory analysis, the potential regulatory mechanisms of key genes in the HCC microenvironment were explored, and their potential as therapeutic targets was preliminarily evaluated. This study aimed to provide

bioinformatic insights into the metabolite-mediated cell communication mechanisms in the HCC microenvironment and offer preliminary clues for potential intervention strategies.

Materials and methods

Data acquisition

scRNA-seq data were obtained from the Gene Expression Omnibus (GEO) database (https://www.ncbi.nlm.nih.gov/geo/) under accession number GSE149614 (platform GPL24676), comprising ten primary tumor (PT) and non-tumor liver (NTL) samples from patients with HCC. Bulk RNA sequencing (bulk RNA-seq) data were also retrieved from the GEO database. The training cohort GSE76427 (GPL10558) contained 115 tumor samples and 52 non-tumor liver samples, and the validation cohort GSE115018 (GPL20115) contained 12 tumor samples and 12 non-tumor liver samples.

Single-cell data preprocessing and cell type annotation

Quality control was performed using the R package Seurat (v5.3.0)[11]. Genes expressed in fewer than three cells were removed. Cells were retained if they satisfied the following criteria: 200–4,000 detected genes (nFeature_RNA), mitochondrial gene fraction < 15%, and total unique molecular identifier (UMI) counts between 500 and 10,000. Doublets were identified and excluded. After normalization with the NormalizeData function, the top 3,000 highly variable genes were selected via the FindVariableFeatures function. Principal component analysis (PCA) was performed on scaled data, and the number of significant components was determined by JackStraw testing and elbow plot evaluation. Cells were clustered using the FindNeighbors and FindClusters functions (resolution = 0.8) and visualized by uniform manifold approximation and projection (UMAP). Marker genes for each cluster were identified with the FindAllMarkers function. Cell types were annotated by matching these markers to established lineage-defining genes from published references[12-15].

Metabolite-mediated cell-cell communication inference

Metabolite-mediated cell-cell communication (mCCC) was inferred using the MEBOCOST framework, which integrates a curated knowledge base of extracellular metabolites, metabolic enzymes, and metabolite sensors. Expression values of enzyme and sensor genes were extracted from the scRNA-seq matrix and averaged per cell type. For each sender–receiver cell-type pair, a communication score was computed as the product of the mean enzyme expression in the sender population and the mean sensor expression in the receiver population. Statistical significance was evaluated by permuting cell-type labels to construct a null distribution. Detected communication events were visualized as network diagrams and quantified per cell type in bar charts. The mCCC patterns were compared between the PT and NTL groups. Significant metabolite–sensor pairs were further refined by incorporating single-cell metabolic flux estimates, with efflux as secretion evidence and influx as uptake evidence. These flux data were jointly constrained with the enzyme–sensor co-expression significance to yield a final list of high-confidence mCCC events, each annotated with the metabolite, sender cell type, receiver cell type, sensor gene, and supporting statistics. The prioritized receiver cell type was designated as the key cell type for subsequent analyses.

High-dimensional weighted gene co-expression network analysis

Gene co-expression modules within the key cell type were identified by hdWGCNA using the R package hdWGCNA (v0.4.5)[16]. To address the sparsity of scRNA-seq data, a metacell expression matrix was constructed by aggregating cells according to cell type, condition, and sample of origin. A soft-thresholding power was selected based on scale-free topology fitting, and a co-expression network was built from the metacell matrix.

Module eigengene-based activity was compared across cell types, and the module most strongly associated with the key cell type was identified. Genes within this module were collectively termed module genes.

Differential expression analysis and candidate gene identification

Differentially expressed genes (DEGs) between HCC tumor and non-tumor liver samples were identified in the training cohort GSE76427 using the limma package (v3.56.2)[17]. Significance thresholds were set at |log2 fold change (FC)| > 0.5 and adjusted $P < 0.05$. Upregulated DEGs were intersected with the module genes derived from hdWGCNA using the VennDiagram package (v1.7.3)[18] to define a candidate gene set for downstream selection.

Machine learning-based feature selection

Five classification algorithms were employed to extract robust feature genes from the candidate gene set, using tumor versus non-tumor status as the binary outcome. First, an extreme gradient boosting (XGBoost) model was trained with the xgboost package (v2.0.3.1)[19], and genes with Gain values above the median were retained. Second, support vector machine–recursive feature elimination (SVM-RFE) was performed using the e1071 package (v1.7.14)[20] with a linear kernel; five-fold cross-validation was applied to identify the optimal feature subset based on the lowest misclassification error. Third, a random forest (RF) model was constructed with the randomForest package (v4.7.1.1)[21] (ntree = 500), and genes with MeanDecreaseGini > 1.0 were selected. Fourth, a gradient boosting machine (GBM) was fitted using the gbm package (v2.1.9) [22], and genes were ranked by relative influence. Fifth, a Naive Bayes (NB) classifier was trained with the e1071 package (v1.7.14), and feature contributions were quantified by a normalized separability metric computed from class-conditional mean and variance estimates. Genes consistently selected by all five algorithms were defined as consensus feature genes. Their expression was validated in both the training and validation cohorts; only those showing statistically significant differential expression with concordant direction in both cohorts were retained as key genes.

Functional enrichment and immune microenvironment analysis

Single-gene gene set enrichment analysis (GSEA) was conducted in the training cohort GSE76427 to characterize pathways associated with key genes. For each key gene, a ranked gene list was generated based on Spearman correlation coefficients **(r)** with all other genes, and GSEA was performed against Kyoto Encyclopedia of Genes and Genomes (KEGG) pathway sets from the Molecular Signatures Database (MSigDB, https://www.gsea-msigdb.org/gsea/msigdb) using the clusterProfiler package (v4.8.3)[23.]
We ensured that the required permissions and documentation were provided in accordance with the journal's guidelines.When using KEGG imagery that we cited this source in the appropriate figure legend, as per the citation guidelines: www.kegg.jp/kegg/kegg1.html[24].
Significant pathways were defined by |normalized enrichment score (NES)| > 1, $P < 0.05$, and false discovery rate (FDR) < 0.25. Subcellular localization of key gene transcripts was characterized using the mRNALocator database (http://rnalocate.org/), and protein interaction networks for key genes were constructed via GeneMANIA (https://genemania.org/). Immune infiltration was quantified by single-sample GSEA (ssGSEA) for 28 immune cell types using the GSVA package (v1.48.3)[25]. Infiltration score differences between HCC tumor and non-tumor liver samples were tested by the Wilcoxon rank-sum test. Pairwise correlations among differentially infiltrated immune cell types, as well as correlations between key gene expression and immune cell infiltration scores, were calculated using Spearman's method ($|r| > 1$, $P < 0.05$).

Single-cell pathway activity and metabolic reprogramming analysis

Cell type-resolved pathway activity across the HCC microenvironment was evaluated using the ReactomeGSA package (v1.16.1)[26]. Single-cell metabolic pathway activity was scored by the AUCell method implemented in the scMetabolism package (v0.2.1)[27]. A panel of KEGG metabolic pathways relevant to HCC was selected, including glycolysis/gluconeogenesis, pyruvate metabolism, the tricarboxylic acid (TCA) cycle, the pentose phosphate pathway, fatty acid metabolism, glycerolipid and glycerophospholipid metabolism, sphingolipid metabolism, glutathione metabolism, branched-chain amino acid metabolism, and oxidative phosphorylation. Pathway activity scores were compared between tumor and non-tumor groups within each cell type. Transcription factor (TF) activity in tumor cells was inferred using the DoRothEA regulon resource (v1.14.1)[28]coupled with the VIPER algorithm (v1.36.0)[29].

Pseudotime trajectory analysis

To dissect transcriptional heterogeneity within the key cell type, subclustering was performed following the same Seurat workflow. Pseudotime trajectory reconstruction was carried out using the Monocle2 package (v2.26.0)[30.] Ordering genes were selected based on differential expression, and dimensionality reduction was performed via the DDRTree algorithm. Cells were arranged along a branching trajectory reflecting cell state transitions. Expression levels of key genes were projected onto the pseudotime axis to characterize their dynamic changes during state progression.

Drug-target prediction and molecular docking

Potential binding interactions between candidate compounds and proteins encoded by key genes were predicted using GraphBAN, a graph neural network framework that jointly encodes molecular graph structures and protein sequence features. Predictions were independently generated from models pre-trained on BindingDB, KIBA, and Biosnap datasets. Compound–target pairs unanimously supported by all three models were retained, ranked by mean prediction score, and the top 10 compounds were selected. Binding affinity was subsequently validated by molecular docking using CB-Dock2 (https://cadd.labshare.cn/cb-dock2/). Complexes with binding energy ≤ −5 kcal/mol were considered to exhibit favorable affinity.

Molecular dynamics simulation

Molecular dynamics (MD) simulations were conducted using GROMACS (v2024.4) [31] to evaluate the dynamic stability of docked compound–protein complexes. The AMBER99SB-ILDN force field and TIP3P water model were applied. Each complex was solvated in a cubic box with a minimum solute-to-boundary distance of 1 nm, and counterions were added to neutralize the system. Energy minimization was performed by the steepest descent algorithm. The system was equilibrated sequentially under canonical ensemble (NVT) and isothermal-isobaric ensemble (NPT) conditions at 300 K with V-rescale thermostat coupling for 100 ps each. Production MD simulations were run for 100 ns. System stability was assessed by analyzing root mean square deviation (RMSD), root mean square fluctuation (RMSF), total energy, and hydrogen bond occupancy over the trajectory.

Immunohistochemistry (IHC) analysis

HCC tissues and adjacent cirrhotic tissues were collected from 82 patients with hepatic cirrhosis with HCC who underwent hepatectomy between January 2016 and December 2021 at the Fourth Hospital of Hebei Medical University. All patients were followed up until December 2024. We confirmed that informed consent was obtained from all subjects and all methods were carried out in accordance with relevant guidelines and regulations. The study received approval from the ethics committee of the Fourth Hospital of Hebei Medical University (certificate no. 2021KY103).To validate the protein-level expression

of the key genes identified by transcriptomic analyses, formalin-fixed, paraffin-embedded (FFPE) sections of HCC tumor tissues and paired adjacent non-tumor liver tissues were subjected to immunohistochemistry (IHC). After deparaffinization, rehydration, and antigen retrieval, sections were incubated with primary antibodies against SNX27, PEA15 and HMOX1 at 4 °C overnight, followed by incubation with an enzyme-labeled secondary antibody and visualization with 3,3′-diaminobenzidine (DAB). Sections were counterstained with hematoxylin, dehydrated, and mounted. Staining was scored semi-quantitatively by two independent pathologists in a blinded manner based on the proportion of positive cells and staining intensity, and differences between tumor and adjacent tissues were assessed statistically. The slides were then washed and incubated with a secondary antibody according to the manufacturers' instructions, followed by incubation with diaminobenzidine chromogen. Images were captured by using an Olympus BX51T-PHD-J11 (Olympus, Tokyo, Japan). Immunohistochemical staining was quantified with Image-Pro Plus 5.1 for Windows software (Media Cybernetics Inc., Rockville, MD, US) by using the measurement function. The number of positive cells and the colour intensity of positive cells were obtained, and the immunohistochemistry score (IHS) was calculated as follows: A, positive cell number grading: 0–1% = 0, 1–10% = 1, 10–50% = 2, 50–80% = 3, and 80–100% = 4; B, colour intensity of positive cells grading: grade 0 (negative), 1 (weak positive), 2 (positive), and 3 (strong positive); IHS = A × B. IHS > 100 was defined as positive (+), and IHS ≤ 100 was defined as negative (-).

Statistical analysis

All computational analyses were performed in R (v4.3.3). Statistical tests were two-tailed, and $P < 0.05$ (or adjusted P where applicable) was considered statistically significant.

Results

Macrophages were identified as the primary receiver of metabolite-mediated intercellular communication in HCC

Following quality control and normalization (**Figure S1a**), the top 3,000 highly variable genes were selected for dimensionality reduction (**Figure S1b**), and the top 30 principal components were retained for clustering (**Figure S1c**). A total of 21 clusters were identified (**Figure S1d**), and they were annotated into ten cell types: T cells, natural killer cells, B cells, plasma cells, macrophages, dendritic cells, mast cells, hepatocytes, endothelial cells, and fibroblasts (**Fig. 1a-b**). MEBOCOST analysis detected extensive mCCC events in HCC samples, with mltiple cell types functioning simultaneously as senders and receivers (**Fig. 1c**). Quantification showed that PT-hepatocytes ranked highest as senders (65 events), while PT-macrophages were prominent in both sender (58 events) and receiver (46 events) capacities (**Fig. 1d**). Comparison between the PT and NTL groups further revealed that multiple PT-enriched communication events repeatedly converged on macrophages as receivers (**Fig. 1e**, **Table S1**). Among 32 detected metabolites, the iron and farnesyl pyrophosphate axes were particularly prominent in macrophage-directed events, alongside L-glutamine, D-mannose, and cholesterol (**Table 1**). These results established macrophages as the primary receiver population within the HCC mCCC network.

Co-expression network and differential expression analyses yielded 22 mCCC-related candidate genes

To identify gene modules relevant to the mCCC receiver population, hdWGCNA was performed. A soft-thresholding power of 7 ($R^2 > 0.85$) was selected (**Fig. 2a**), and six co-expression modules were identified (**Fig. 2b-d**), with varying inter-module correlations observed (**Fig. 2e**). The blue module showed the highest eigengene correlation with macrophages and was designated as the key module, comprising 666 module genes (**Fig.**

2f, **Table S2**). Separately, differential expression analysis of the training cohort GSE76427 identified 1,738 DEGs between HCC tumor and non-tumor liver samples, including 745 upregulated and 993 downregulated genes (**Fig. 2g-h**, **Table S3**). The intersection of the upregulated DEGs with the key module genes yielded 22 candidate genes (**Fig. 2i**, **Table S4**), representing potential molecular effectors linking mCCC signals to transcriptomic alterations.

Machine learning consensus and cross-cohort validation defined SNX27 and PEA15 as key genes

Five machine learning algorithms were applied to the 22 candidate genes to extract robust discriminative features. XGBoost retained 11 genes with above-median Gain values (**Fig. 3a**). SVM-RFE identified an optimal six-gene subset at the lowest cross-validation error (accuracy = 0.9461) (**Fig. 3b**). RF selected 20 genes with MeanDecreaseGini > 1.0 (**Fig. 3c**). GBM retained 11 genes by relative influence (**Fig. 3d**). NB identified 11 genes by normalized separability scores (**Fig. 3e**). Intersection of all five algorithms yielded four consensus genes: SNX27, WDR45B, PEA15, and JKAMP (**Fig. 3f**). Expression validation showed that all four consensus genes were significantly upregulated in tumor samples within the training cohort ($P < 0.0001$). In the independent validation cohort, however, only SNX27 and PEA15 maintained significant overexpression ($P < 0.001$), whereas WDR45B and JKAMP failed to reach significance. SNX27 and PEA15 were therefore defined as key genes (**Fig. 3g**).

Key genes converged on lipid metabolism suppression and apoptosis-related signaling

Single-gene GSEA was performed to explore the functional context of key genes. PEA15 was negatively enriched in fatty acid metabolism, valine leucine and isoleucine degradation, retinol metabolism, tryptophan metabolism, and complement and coagulation cascades, while positively enriched in cell cycle, ribosome, and DNA replication (**Fig. 4a**, **Table S5**). SNX27 was negatively enriched in fatty acid metabolism, complement and coagulation cascades, retinol metabolism, and tryptophan metabolism, and positively enriched in spliceosome and DNA replication (**Fig. 4b**, **Table S6**). Both key genes shared negative enrichment in fatty acid metabolism and branched-chain amino acid degradation, and positive enrichment in cell cycle and RNA processing pathways (**Fig. 4c**). Subcellular localization analysis revealed that both SNX27 and PEA15 transcripts were predominantly nuclear, with additional cytoplasmic and extracellular distribution (**Fig. 4d**). Protein interaction network analysis via GeneMANIA showed that both key genes occupied central positions and were functionally linked to CASP8, CASP10, FADD, CFLAR, MAPK1, and MAPK3. Enrichment of this network was dominated by extrinsic apoptotic signaling and cysteine-type endopeptidase regulation (**Fig. 4e**). The convergence of both key genes on lipid metabolic and apoptotic pathways raised the possibility that these genes might participate in metabolic signal transduction within the tumor microenvironment, though the directionality of this relationship requires further validation.

Key gene expression was inversely associated with immune cell infiltration in HCC

To assess the relationship between key genes and the immune landscape, ssGSEA-based immune infiltration profiling was performed. Marked heterogeneity was observed between HCC tumor and non-tumor liver tissues (**Fig. 5a**). Tumor samples exhibited significantly reduced infiltration of multiple immune populations, including activated B cells, activated dendritic cells, effector memory CD8 T cells, macrophages, myeloid-derived suppressor cells (MDSCs), neutrophils, regulatory T cells, and type 1 T helper cells ($P < 0.0001$) (**Fig. 5b**). These depleted populations were strongly positively correlated with each other; in particular, macrophages showed significant correlations with MDSCs, effector memory

CD8 T cells, and regulatory T cells ($r > 0.7$, $P < 0.001$) (**Fig. 5c**, **Table S7**). Correlation analysis revealed that SNX27 was inversely correlated with neutrophils, eosinophils, effector memory CD8 T cells, macrophages, regulatory T cells, and mast cells ($r < -0.4$, $P < 0.001$). PEA15 was inversely correlated with neutrophils ($r = -0.38$, $P < 0.001$) and eosinophils ($r = -0.39$, $P < 0.001$), while positively correlated with central memory CD4 T cells ($r = 0.35$, all $P < 0.001$) (**Fig. 5d**). These inverse associations between key gene expression and immune infiltration suggest that SNX27 and PEA15 might coincide with immunosuppressive remodeling in the HCC microenvironment.

Macrophages exhibited metabolic reprogramming with dynamic key gene expression along differentiation trajectories

To further characterize the metabolic and transcriptional features of macrophages, pathway-level and single-cell metabolic analyses were performed. Hepatocytes were enriched in NFE2L2-regulated inflammation-associated genes and developmental biology pathways, while macrophages were enriched in activated NTRK2 signals through FYN, and NTRK2 activates RAC1 (**Fig. 6a**). Single-cell metabolic profiling revealed broadly enhanced metabolic activity in tumor samples, with hepatocytes and macrophages exhibiting the most pronounced alterations. Tumor macrophages specifically showed upregulated glycosphingolipid biosynthesis—globo and isoglobo series, glycan degradation, riboflavin metabolism, and valine, leucine and isoleucine biosynthesis (**Fig. 6b-6c**). TF activity inference revealed elevated STAT6, KLF4, RFX5, FLI1, ESR2, and CDX2 activity in macrophages compared with other cell types (**Fig. 6d**). Subclustering partitioned macrophages into six subtypes: Macro_MARCO, Macro_BAG3, Macro_VCAN, Macro_CXCL9, Macro_MMP9, and Macro_TOP2A (**Fig. 6e**, **Figure S2**). Pseudotime trajectory reconstruction revealed a branching differentiation structure, with Macro_VCAN at an early state and Macro_MARCO at a terminal state (**Fig. 6f**). PEA15 expression remained relatively stable along the trajectory, whereas SNX27 exhibited a gradual upward trend as pseudotime progressed (**Fig. 6g**). The progressive increase of SNX27 along differentiation trajectories suggested that the capacity of macrophages to process mCCC signals might vary with cellular differentiation state.

Trabectedin formed stable complexes with both key gene-encoded proteins

To identify potential compounds capable of modulating key genes, drug-target interaction prediction was performed. GraphBAN analysis identified high-confidence candidate compounds for both SNX27 and PEA15, with the top 10 ranked by combined prediction score (**Fig. 7a**). Trabectedin achieved the highest score for SNX27 and was also among the top candidates for PEA15. Farnesyl pyrophosphate, the prominent metabolite identified in the mCCC analysis, was included as a reference docking ligand to compare pharmacological agents against endogenous metabolite binding. Molecular docking demonstrated that SNX27–Trabectedin (−10.2 kcal/mol) and PEA15–Trabectedin (−9.7 kcal/mol) exhibited substantially more favorable binding energies than their respective farnesyl pyrophosphate complexes (−6.5 and −7.0 kcal/mol) (**Table 2**, **Fig. 7b–7e**). MD simulations over 100 ns assessed the dynamic stability of these complexes. The PEA15–farnesyl pyrophosphate complex displayed conformational instability, with RMSD rising to approximately 4 nm by 80 ns. In contrast, the SNX27–Trabectedin, SNX27–farnesyl pyrophosphate, and PEA15–Trabectedin complexes maintained stable conformations at approximately 1 nm (**Fig. 7f**). RMSF profiles confirmed minor residue-level fluctuations across all systems (**Fig. 7g**), and total energy remained stable without drift (**Fig. 7h**). Hydrogen bond analysis showed persistent bonding in both SNX27 complexes, while PEA15 complexes exhibited intermittent hydrogen bond formation (**Fig. 7i**). These computational results indicated that trabectedin formed thermodynamically favorable and conformationally stable interactions with both key gene-encoded proteins, showing

stronger binding affinity and stability than the endogenous metabolite. These findings provided preliminary evidence that pharmacological intervention targeting SNX27 and PEA15 might represent a potential strategy to modulate metabolite-mediated communication in the HCC microenvironment.

Immunohistochemistry confirmed the protein-level expression of key genes in HCC tissues

Immunostaining of SNX27, PEA15 and HMOX1 were predominantly localized in the cytoplasm and nucleus, and three proteins exhibited stronger staining intensity and a higher proportion of positive cells in HCC tumor tissues than in adjacent non-tumor liver tissues(**Fig. 8a**). The expression intensities of SNX27 and PEA15 were positively correlated with that of HMOX1; among them, SNX27 had the highest correlation with HMOX1(R^2=0.6,*P*=0.001)(**Fig. 8b**).The expression of SNX27, PEA15 and HMOX1 were strongly associated with tumor differentiation, stage, and prognosis. The results indicate that patients with positive expression of SNX27, PEA15 and HMOX1 exhibited poorly differentiated tumors, advanced stage disease, and worse prognosis(**Fig. 8c,d**).This protein-level elevation was concordant with the transcriptomic upregulation of SNX27 and PEA15 observed in the bulk RNA-seq cohorts, thereby providing complementary evidence supporting the identification of these two key genes.

Discussion

This study integrated public single-cell RNA sequencing data and bulk transcriptome data to systematically analyze the metabolite-mediated intercellular communication network within the HCC microenvironment, identified macrophages as the main receiver population, and through the integration of co-expression network analysis, differential expression analysis, and cross-validation of multi-algorithm machine learning, two key genes, sorting nexin 27 (SNX27) and phosphoprotein enriched in astrocytes 15 (PEA15), were identified. Subsequently, through functional enrichment, immune microenvironment assessment, single-cell metabolic analysis, and trajectory reconstruction, the potential regulatory role of key genes in the HCC microenvironment was preliminarily explored, and the targeting potential of trabectedin was evaluated through molecular docking and molecular dynamics simulation.

Metabolites such as iron, farnesyl pyrophosphate (FPP), and glutamine may serve as candidate mCCC signals received by TAMs, thereby contributing to immunosuppressive polarization and HCC progression together with CD8+ T-cell dysfunction and myeloid-cell remodeling[32-34]. MEBOCOST analysis revealed that macrophages were the main receivers of mCCC in HCC, indicating that macrophages are not passive infiltrating cells but important integration nodes of tumor metabolic signals. Existing studies have shown that TAMs are the core immune components in the tumor microenvironment of HCC and tend to polarize toward the M2-like tumor-promoting phenotype to create a tumor-promoting microenvironment[35-37]. Meanwhile, metabolites such as iron, FPP, L-glutamine, D-mannose, and cholesterol identified in this study have all been associated with metabolic reprogramming, immunosuppression or tumor-promoting effects of HCC in previous studies: Iron accumulation can weaken the effector function of CD8+ T cells[32], and GLRX3 can affect the immune microenvironment of HCC through iron metabolism[38]. FPP is involved in mitochondrial regulation of immune cells and is related to the expression regulation of TAZ in HCC[39,40]. Glutamine metabolism is closely related to mTOR activation, epigenetic regulation and the occurrence of HCC[33,41]. More importantly, there is direct evidence that metabolites can promote TAM polarization through intercellular communication. For instance, D-lactic acid can drive M2 polarization, and inositol can activate M2-type macrophages through SLC5A3[34,42].

Together, these findings suggest that in HCC, the release of multiple metabolites may continuously act on TAMs and promote their immunosuppressive polarization.

This study integrated co-expression network analysis, differential expression analysis, and multi-algorithm machine learning cross-validation to obtain four consensus genes. Among them, SNX27 and PEA15 maintained significant upregulation in the independent validation cohort, while WDR45B and JKAMP did not reach significance; therefore, SNX27 and PEA15 were defined as key genes. SNX27 possesses a unique PDZ structural domain that participates in the recycling of endocytic proteins from endosomes to the plasma membrane, and has been demonstrated to be associated with mTORC1 activation and cell survival under nutrient-deficient conditions[43]; in HCC circ_SNX27 also promotes tumor proliferation and invasion via the miR-637/FGFR1 axis[44]. PEA15 is a phosphoprotein containing a death effector domain, which can regulate the extrinsic apoptotic pathways related to Caspase-8, FADD, and CFLAR, and affect the behavior of tumor cells through ERK nucleocytoplasmic transport. Its cancer-promoting effect has been supported in various solid tumors and has also been confirmed in HCC to promote cell proliferation and migration by stabilizing HIF1A signaling[45-48]. The GSEA results of PEA15 are highly similar to those of SNX27, as both are connected to CASP8, CASP10, FADD, CFLAR, MAPK1, and MAPK3 in the protein interaction network, collectively enriched in the extrinsic apoptosis signaling pathway.The verification in our own database also confirmed SNX27, PEA15 and HMOX1 exhibited stronger expression in HCC tumor tissues,and these genes higher expression were strongly aexhibited poorly differentiated tumors, advanced stage disease, and worse prognosis. In TME, Heme Oxygenase 1 (HMOX1) was an important marker of macrophages, HMOX1 promoted the differentiation of macrophages into M2 types[49,50].Our research also confired the intensities of SNX27 and PEA15 were positively correlated with that of HMOX1. SNX27 and PEA15 might represent molecular nodes associated with macrophage responses to metabolite-derived signals rather than direct activators of macrophages; they may translate exogenous metabolic stimuli into transcriptional responses that are favorable for cell survival, proliferation, and tumor maintenance, and jointly participate in the regulation of the HCC microenvironment.

Our results showed that SNX27 exhibits negative correlations with multiple myeloid and lymphocyte infiltration signatures, while PEA15 shows a negative correlation with neutrophils but a positive correlation with central memory CD4+ T cells, indicating that these two key genes are closely associated with the immune infiltration pattern in HCC. Previous research has demonstrated that immunosuppression in HCC is not solely attributable to individual cell types but is collectively shaped by myeloid cells such as tumor-associated macrophages (TAMs), neutrophils, and myeloid-derived suppressor cells (MDSCs). For example, acetyl-CoA promotes neutrophil infiltration via the CXCL1 mechanism[51]; CRKL-mediated neutrophil proliferation is linked to anti-PD-1 resistance[52]; and interventions targeting TAM metabolic programs, including the APOC1/NUPR1-histone lactylation axis, OXCT1, and SRSF10 have shown potential to reshape the immune microenvironment of HCC[53-56]. This pattern further suggests that the abnormal upregulation of SNX27 and PEA15 is not merely an intrinsic event within tumor cells, but more likely reflects or mediates the remodeling of a macrophage-dominated immunosuppressive microenvironment. These two proteins may serve as correlation-based molecular bridges rather than experimentally validated causal mediators linking mCCC signaling to immune infiltration imbalance.

Single-cell metabolic analysis and pseudotime trajectory analysis revealed that tumor macrophages exhibited enhanced metabolic activity and a differentiation trajectory from Macro_VCAN to Macro_MARCO. In this trajectory, PEA15 expression was relatively

stable, while SNX27 gradually increased with the advancement of pseudotime. This dynamic pattern suggests that SNX27 may not merely be a concomitant marker but is closely related to the functional maturation of macrophages. Concurrently, STAT6 and KLF4 activity increased in macrophages, both of which are recognized as key regulators of M2 polarization[57-60]. These observations suggest that the gradual upregulation of SNX27 may be involved in macrophage transition from an early state to a mature, immunosuppressive receiver state, and enhance their responsiveness to tumor-derived metabolites by influencing membrane receptor recycling, nutrient sensing or metabolic signal-processing capabilities. In contrast, PEA15 is more likely to act as a more stable synergistic molecule, maintaining the signal homeostasis downstream of this process.

GraphBAN prioritized trabectedin as a high-scoring candidate compound for SNX27 and PEA15. Trabectedin is the first approved marine-derived antitumor drug, whose mechanism involves DNA binding, transcriptional regulation, and TME modulation, and has been utilized in various malignant tumors including soft tissue sarcoma and ovarian cancer[61]. Combination with doxorubicin can significantly prolong survival in advanced leiomyosarcoma[62]. In this study, GraphBAN predictions, molecular docking, and molecular dynamics simulations collectively suggested that trabectedin showed favorable predicted affinity and conformational stability toward both SNX27 and PEA15, with predicted binding performance superior to that of the endogenous reference ligand FPP. Given that trabectedin is known to act on tumor-associated myeloid cells and their microenvironment, these findings further support the hypothesis that trabectedin may not only affect tumor cells but also alter macrophages' ability to receive and integrate metabolic signals by interfering with the SNX27/PEA15-related molecular network, thereby inhibiting mCCC-driven immunosuppressive microenvironment remodeling.

This study has the following limitations. First, all data used in this study were obtained from public databases, and sample-source heterogeneity may have affected the results. Second, the mCCC events inferred by MEBOCOST reflect statistical associations rather than direct evidence of genuine causal metabolic signaling between cells. Third, the generalizability of machine learning models needs to be externally verified by larger-scale independent cohorts. Fourth, all findings are based on bioinformatics analysis, and the functional roles of SNX27 and PEA15 in mCCC regulation, as well as the targeting efficacy of trabectedin, have not yet been validated in vitro cellular experiments or animal models. Future work should address these limitations through mechanistic experiments and larger independent clinical cohorts.

Conclusions

Through systematic bioinformatics analysis, this study delineated the mCCC network architecture in HCC and identified macrophages as the primary receivers. By integrating multi-level analysis, SNX27 and PEA15 were identified as key genes related to mCCC, revealing their potential associations with lipid metabolism, apoptotic signaling, and the immune microenvironment. These findings provide preliminary computational support for trabectedin as a potential candidate compound. Future research should focus on verifying the specific roles of SNX27 and PEA15 in mCCC signaling through functional experiments, evaluating their prognostic value in independent clinical cohort studies, and validating the targeting effects of trabectedin in cell and animal models. Overall, this study provides directional insights for further investigation into the metabolic communication mechanisms within the HCC microenvironment and provides a preliminary basis for the exploration of related therapeutic targets.

Abbreviations

Abbreviation	Full name

HCC	Hepatocellular carcinoma
TME	Tumor microenvironment
mCCC	Metabolite-mediated cell-cell communication
MEBOCOST	Metabolite-mediated cell-cell communication scoring tool
scRNA-seq	Single-cell RNA sequencing
bulk RNA-seq	Bulk RNA sequencing
GEO	Gene Expression Omnibus
PT	Primary tumor
NTL	Non-tumor liver
hdWGCNA	High-dimensional weighted gene co-expression network analysis
DEGs	Differentially expressed genes
GSEA	Gene set enrichment analysis
KEGG	Kyoto Encyclopedia of Genes and Genomes
ssGSEA	Single-sample gene set enrichment analysis
TAMs	Tumor-associated macrophages
MDSCs	Myeloid-derived suppressor cells
FPP	Farnesyl pyrophosphate
TF	Transcription factor
MD	Molecular dynamics
RMSD	Root mean square deviation
RMSF	Root mean square fluctuation
SVM-RFE	Support vector machine-recursive feature elimination
RF	Random forest
GBM	Gradient boosting machine
NB	Naive Bayes

Acknowledgments

The authors would like to thank the staff of the Department of Gastroenterology and Hepatology, The Fourth Hospital of Hebei Medical University (Shijiazhuang, China), for their technical support and insightful discussions.

Author Contributions

Shi JF, Zhang H,and Yin F Writing – review & editing, Conceptualization, Methodology, Project administration, Han X and Wang JF Writing – original draft, Conceptualization, Methodology, Shi JF supervised the study and revised the manuscript. All authors have read and approved the final manuscript.

Funding

This study was supported by the Hebei Natural Science Foundation (grant number: H2021206425) and the Medical Science Research Project of Hebei Provincial Health and Family Planning Commission of China (Grant No. 20220156).

Competing Interests

The author(s) declare(s) that there is no conflict of interest regarding the publication of this article.

Data Availability

The datasets analysed in this study are available in the GEO repository (https://www.ncbi.nlm.nih.gov/geo/). The specific datasets used include GSE149614, GSE76427 and GSE115018.

Ethics Approval and Consent to Participate

The study received approval from the ethics committee of the Fourth Hospital of Hebei Medical University (certificate no. 2021KY103).

Consent for Publication

Not applicable.

Supplementary Materials

Figure S1-S2

Table S1-S7

References

1.Nagaraju, G.P., Dariya, B., Kasa, P., et al. Epigenetics in hepatocellular carcinoma. *Seminars in Cancer Biology*. 86,622-632 (2022).

2.Alawyia, B., Constantinou, C. Hepatocellular carcinoma: A narrative review on current knowledge and future prospects. *Current Treatment Options in Oncology*. 24,711-724 (2023).

3.Qiu, Q, Yin, H, Zhang, L, et al. SLC25A39 regulates Hedgehog signaling to promote tumor progression and sorafenib resistance in hepatocellular carcinoma. *Sci Rep.* 15 (1), 36061(2025).

4.Su, X., Yan, X., Zhang, H. The tumor microenvironment in hepatocellular carcinoma: mechanistic insights and therapeutic potential of traditional Chinese medicine. *Mol Cance*r.24, 173 (2025).

5.Chen, C., Wang, Z., Ding, Y., Qin, Y. Tumor microenvironment-mediated immune evasion in hepatocellular carcinoma. *Front Immunol*. 14,1133308 (2023).

6.Gao, B., Lu, Y., Lai, X., et al. Metabolic reprogramming in hepatocellular carcinoma. *Front Immunol*. 16,1592837 (2025).

7.Park, S., Hall, M.N. Metabolic reprogramming in hepatocellular carcinoma: mechanisms and therapeutic implications. *Exp Mol Med*. 57, 515-523 (2025).

8.Zhu, H., Li, J., Zhang, J., et al. Molecular regulatory network of glycolytic reprogramming in hepatocellular carcinoma and its clinical implications. *Biol Proced Online*. 27, 51(2025).

9.Wang, C., Zhang, X., Yu, J., et al. Spotlights on extracellular vesicles in hepatocellular carcinoma diagnosis and treatment: An update review. *Front. Bioeng. Biotechnol.* 11, 1215518 (2023).

10.Zheng, R., Zhang, Y., Tsuji, T., et al. MEBOCOST maps metabolite-mediated intercellular communications using single-cell RNA-seq. *Nucleic Acids Res.* 53(12), gkaf569(2025).

11.Satija, R., Farrell, J.A., Gennert, D., et al. Spatial reconstruction of single-cell gene expression data. *Nat Biotechnol*. 33, 495-502(2015).

12.Jin H., Kim, W., Yuan, M., et al. Identification of SPP1+ macrophages as an immune suppressor in hepatocellular carcinoma using single-cell and bulk transcriptomics. *Front Immunol.* 15,1446453 (2024,).

13.Sun, Y., Wu, L., Zhong, Y. et al. Single-cell landscape of the ecosystem in early-relapse hepatocellular carcinoma. *Cell.* 184(2), 404-421.e16 (2021). https://doi.org/10.1016/j.cell.2020.11.041.

14.Chen, Z., Wang, X., Wu, H. et al. X-box binding protein 1 as a key modulator in "healing endothelial cells", a novel ec phenotype promoting angiogenesis after mcao. *Cell Mol Biol Lett*. 27, 97(2022).

15.Liu, H., Li, X., Zhang, C. et al. GJB2 Promotes HCC Progression by Activating Glycolysis Through Cytoplasmic Translocation and Generating a Suppressive Tumor Microenvironment Based on Single Cell RNA Sequencing. *Adv Sci (Weinh).* 11(39), e2402115(2024).

16.Morabito, S.; Reese, F.; Rahimzadeh, N. et al. Hdwgcna identifies co-expression networks in high-dimensional transcriptomics data. *Cell Reports Methods*. 3(6), 100498 (2023).
17.Ritchie, M.E.; Phipson, B.; Wu, D.; et al. limma powers differential expression analyses for RNA-sequencing and microarray studies,. *Nucleic Acids Res*. 43(7):e47(2015).
18.Chen, H., Boutros, P.C. Venndiagram: A package for the generation of highly-customizable venn and euler diagrams in r. *BMC Bioinformatics*. 12,35(2011).
19.Hou, N., Li, M., He, L. et al. Predicting 30-days mortality for MIMIC-III patients with sepsis-3: a machine learning approach using XGboost. *J Transl Med.* 18, 462 (2020).
20.Yoon, S., Kim, S. Adaboost-based multiple svm-rfe for classification of mammograms. *BMC Med Inform Decis Mak*. 9 Suppl 1, S1(2009).

21.Lyu, N., Wu, J., Dai, Y. et al. Identification of feature genes and molecular mechanisms involved in cell communication in uveal melanoma through analysis of single-cell sequencing data. *Oncol Lett.* 28(5), 503 (2024).
22.Tang, L., Wang, X., Xia, Z. et al. ATP6AP1 drives pyroptosis-mediated immune evasion in hepatocellular carcinoma: a machine learning-guided therapeutic target. *Discov Oncol.* 16, 616 (2025).
23.Yu, G., Wang, L.G., Han, Y. et al. Clusterprofiler: An r package for comparing biological themes among gene clusters. *Omics*. 16(8), 284-287 (2012).
24.Kanehisa, M., Sato, Y., Kawashima, M. et al. KEGG as a reference resource for gene and protein annotation. *Nucleic Acids Res*. 44, D457-D462 (2016).
25.Hänzelmann, S., Castelo, R., Guinney, J. GSVA: gene set variation analysis for microarray and RNA-seq data. *BMC Bioinformatics.* 14, 7 (2013).
26.Griss, J., Viteri, G., Sidiropoulos, K. et al. ReactomeGSA-Efficient Multi-Omics Comparative Pathway Analysis. *Mol Cell Proteomics.*19, 2115-2125 (2020).
27.Wu, Y.; Yang, S.; Ma, Ji. et al. Spatiotemporal Immune Landscape of Colorectal Cancer Liver Metastasis at Single-Cell Level. *Cancer Discov.* 12(1), 134–153(2022).
28.Garcia-Alonso, L., Holland, C.H., Ibrahim, M.M. et al. Benchmark and integration of resources for the estimation of human transcription factor activities. *Genome Res.* 29(8), 1363-1375 (2019).
29.Alvarez, M.J., Shen, Y., Giorgi, F.M. et al. Functional characterization of somatic mutations in cancer using network-based inference of protein activity. *Nat Genet.* 48,838-847(2016).
30.Qiu, X., Mao, Q., Tang, Y. et al. Reversed graph embedding resolves complex single-cell trajectories. *Nat Methods.* 14, 979-982 (2017).
31.Van Der Spoel, D., Lindahl, E., Hess, B. et al. Gromacs: Fast, flexible, and free. *J Comput Chem*. 26(16), 1701-1718 (2005).
32.Qin, Y., Huo, F., Feng, Z. et al. CD36 promotes iron accumulation and dysfunction in CD8+ T cells via the p38-CEBPB-TfR1 axis in early-stage hepatocellular carcinoma. *Clin Mol Hepatol.* 31(3), 960-980 (2025).
33.Ziki, R.A., Colnot, S. Glutamine metabolism, a double agent combating or fuelling hepatocellular carcinoma. *JHEP Rep.* 6(5),101077 (2024).
34.Han, S., Bao, X., Zou, Y. et al. D-lactate modulates m2 tumor-associated macrophages and reshapes immunosuppression in hepatocellular carcinoma. *Science Advances*. 9(29),eadg2697 (2023).
35.Xu, W., Cheng, Y., Guo, Y. et al. Targeting tumor associated macrophages in hepatocellular carcinoma. *Biochemical Pharmacology*.114990(2022).

36.Liu, Y.T., Mao, Z.W., Ding, Y., Wang ,W.L.Macrophages as targets in hepatocellular carcinoma. *Mol Cancer Ther.* 23(6), 780–790 (2024).
37.Casari, M., Siegl, D., Deppermann, C., Schuppan, D. Macrophages and platelets in *liver fibrosis and hepatocellular carcinoma. Front Immunol. 14, 1277808 (2023).*
38.Li, Y., Chen, Y., Zhang, Y., et al. Integrating multi-omics techniques and in vitro experiments highlights glrx3 in hepatocellular carcinoma iron metabolism. *Front. Immunol.* 5, 1496886 (2024).
39.Zhang, X., Chen, Y., Sun, G., et al. Farnesyl pyrophosphate potentiates dendritic cell migration in autoimmunity through mitochondrial remodelling. *Nat Metab.* 6, 2118–2137 (2024).
40.Saito, Y., Yin, D., Kubota, N. et al. A Therapeutically Targetable TAZ-TEAD2 Pathway Drives the Growth of Hepatocellular Carcinoma via ANLN and KIF23. *Gastroenterology.* 164(7), 1279-1292 (2023).
41.Zhang, Q., Wei, T., Jin, W., et al. Deficiency in SLC25A15, a hypoxia-responsive gene, promotes hepatocellular carcinoma by reprogramming glutamine metabolism. *J Hepatol*. 80(2), :293-308 (2024).
42.Bai, L., Xiong, J., Chen, S. et al. Fbxo22 promotes hepatocellular carcinoma progression via paracrine myo-inositol-induced m2-type polarization of macrophages. *Int J Mol Med.* 57(2),36 (2025).
43.Deb, S., Sun, J. Endosomal sorting protein snx27 and its emerging roles in human cancers. *Cancers*. 15(1),70 (2022).
44.Li, H., Liu, B., Xu, X. et al. Circ_snx27 regulates hepatocellular carcinoma development via mir-637/fgfr1 axis. *Environmental Toxicology*. 37(12),2832-2843 (2022).
45.Peng, Y., Cai, F., Liu, L. et al. Pea15 promotes osteosarcoma progression and cisplatin resistance. *iScience.* 28(11), 113695 (2025).
46.Park, J., Tacam, M.J., Chauhan, G. et al. Nonphosphorylatable PEA15 mutant inhibits epithelial-mesenchymal transition in triple-negative breast cancer partly through the regulation of IL-8 expression. *Breast Cancer Res Treat.*189(2), 333-345 (2021).
47.Li, L., Wang,N., Xiong,Y. et al. Transcription factor fosl1 enhances drug resistance of breast cancer through the dusp7/pea15 pathway. *Mol Cancer Res.* 20(4), 515–526 (2022).
48.Jeong, Y.S., Shin, J.H., Kim, S.M. et al. Proliferation and apoptosis adaptor protein 15 (pea15), a potential oncogenic regulator of vhl and hif1a identified through proteomic analysis in hepatocellular carcinoma. *Cancer Communications*. 46, 0020 (2026).
49.Ito, M., Mimura, K., Nakajima, S. et al. M2 tumor-associated macrophages resist to oxidative stress through heme oxygenase-1 in the colorectal cancer tumor microenvironment. *Cancer Immunol Immunother*. 72, 2233-2244 (2023).
50.Du, Y., Xu, W., Liu, Z. et al. HMOX1+ macrophages determine immunosuppressive microenvironment and immunotherapy efficacy in hepatocellular carcinoma. *Hepatol Commun*. 9, e0815 (2025).
51.Pan, J.J., Xie, S.Z., Zheng, X. et al. Acetyl-CoA metabolic accumulation promotes hepatocellular carcinoma metastasis via enhancing CXCL1-dependent infiltration of tumor-associated neutrophils. *Cancer Lett*. 592, 216903 (2024).
52.Xie, P., Yu, M., Zhang, B.et al. Crkl dictates anti-pd-1 resistance by mediating tumor-associated neutrophil infiltration in hepatocellular carcinoma. *J Hepatol.* 81(1), 93-107 (2024).
53.Hao, X., Zheng, Z., Liu, H. et al. Inhibition of APOC1 promotes the transformation of M2 into M1 macrophages via the ferroptosis pathway and enhances anti-PD1

immunotherapy in hepatocellular carcinoma based on single-cell RNA sequencing. *Redox Biol.* 56, 102463 (2022).
54.Cai, J., Zhang, P., Cai, Y. et al. Lactylation-driven nupr1 promotes immunosuppression of tumor-infiltrating macrophages in hepatocellular carcinoma. *Advanced Science*. 12(20), e2413095 (2025).
55.Zhu, C.X.,Yan, K., Chen, L. et al. Targeting OXCT1-mediated ketone metabolism reprograms macrophages to promote antitumor immunity via CD8+ T cells in hepatocellular carcinoma. *J Hepatol.* 81, 690-703 (2024).
56.Cai, J., Song, L., Zhang, F. et al. Targeting SRSF10 might inhibit M2 macrophage polarization and potentiate anti-PD-1 therapy in hepatocellular carcinoma. *Cancer Commun (Lond).* 44(11), 1231-1260 (2024).
57.Xiao, J., Wang, S., Chen, L. et al. 25-Hydroxycholesterol regulates lysosome AMP kinase activation and metabolic reprogramming to educate immunosuppressive macrophages. *Immunity.* 57(5), 1087-1104 (2024).
58.Zhou, Z., Yao, J., Wu, D. et al. Type 2 cytokine signaling in macrophages protects from cellular senescence and organismal aging. *Immunity.* 57, 513-527e6 (2024).
59.Cao, Y., Xiong, J., Guan, X. et al. Paeoniflorin suppresses kidney inflammation by regulating macrophage polarization. *Phytomedicine.* 116, 154901 (2023).
60.Sun, D., Liu, X., Mao, C. et al. Macelignan targets slc7a11 to induce ferroptosis and reshapes macrophage polarization. *Bioorg Chem.* 169, 109422 (2026).
61.Wang, J., Wang, P., Zeng, Z. et al. Trabectedin in Cancers: Mechanisms and Clinical Applications. *Curr Pharm Des.* 28(24), 1949-1965 (2022).
62.Pautier, P., Italiano, A., Piperno-Neumann, S. et al. Doxorubicin-Trabectedin With Trabectedin Maintenance in Leiomyosarcoma. Obstetrical & Gynecological Survey. 80(4), 230–231 (2025).

Figure Legends:

Fig. 1. Macrophages were identified as the primary receiver of metabolite-mediated intercellular communication in HCC. **(a-b)** The annotation of 21 clusters into ten major cell types, including T cells, natural killer cells, B cells, plasma cells, macrophages, dendritic cells, mast cells, hepatocytes, endothelial cells, and fibroblasts. **(c)** Global metabolite-mediated cell-cell communication (mCCC) network inferred by MEBOCOST across HCC samples, showing sender and receiver relationships among different cell types. **(d)** Quantification of mCCC events for each cell type in sender and receiver roles. **(e)** Differential communication events between the primary tumor (PT) and non-tumor liver (NTL) groups, showing PT-enriched metabolite-mediated signaling preferentially converging on macrophages as receiver cells.

Fig. 2. The co-expression network and differential expression analyses identified 22 candidate genes. **(a)** Soft-threshold power analysis for high-dimensional weighted gene co-expression network analysis (hdWGCNA), showing scale-free topology fit and selection of power = 7. **(b-d)** Hierarchical clustering and module assignment identifying six co-expression modules. **(e)** Correlation heatmap showing relationships among the identified co-expression modules. **(f)** Module–cell type association analysis showing that the blue module had the strongest eigengene correlation with macrophages and was selected as the key module. **(g-h)** Differentially expressed genes between HCC tumor and non-tumor liver tissues in the GSE76427 training cohort. **(i)** Venn diagram showing the intersection between blue module genes and upregulated DEGs, yielding 22 candidate genes.

Fig. 3. Machine learning consensus and cross-cohort validation defined SNX27 and PEA15 as key genes. **(a)** Extreme gradient boosting (XGBoost) feature importance

analysis showing genes with above-median Gain values. **(b)** Support vector machine-recursive feature elimination (SVM-RFE) identifying the optimal feature subset with the lowest cross-validation error. **(c)** Random forest feature selection based on MeanDecreaseGini. **(d)** Gradient boosting machine (GBM) feature ranking by relative influence. **(e)** Naive Bayes (NB) feature ranking based on normalized separability scores. **(f)** Venn diagram showing the overlap among five machine learning algorithms, identifying four consensus genes: SNX27, WDR45B, PEA15, and JKAMP. **(g)** Expression validation of consensus genes in the training and validation cohorts, showing that only SNX27 and PEA15 remained significantly overexpressed in tumors across both cohorts. Statistical significance was defined as follows: ns, not significant; $P < 0.05$, *; $P < 0.01$, **; $P < 0.001$, ***; and $P < 0.0001$, ****.

Fig. 4. Key genes converged on lipid metabolism suppression and apoptosis-related signaling. **(a)** Single-gene gene set enrichment analysis (GSEA) results for PEA15 showing negatively and positively enriched pathways in HCC. **(b)** Single-gene GSEA results for SNX27 showing negatively and positively enriched pathways in HCC. **(c)** Shared enriched pathways between SNX27 and PEA15, highlighting common negative enrichment in lipid metabolic pathways and positive enrichment in cell cycle- and RNA processing-related pathways. **(d)** Subcellular localization analysis of SNX27 and PEA15 transcripts. **(e)** GeneMANIA protein interaction network centered on SNX27 and PEA15.

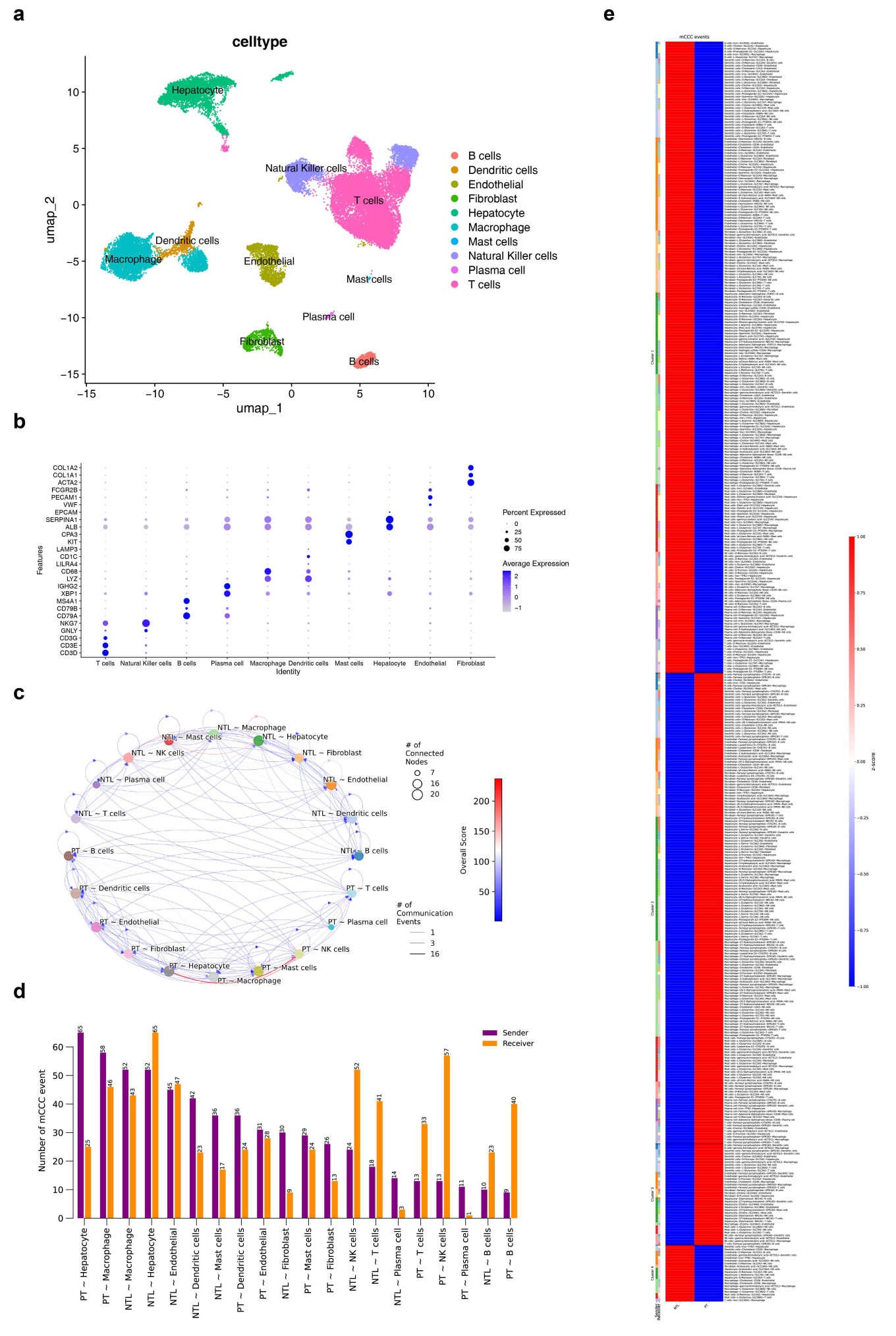
Fig. 5. Key gene expression was inversely associated with immune cell infiltration in HCC. **(a)** Heatmap showing ssGSEA-based immune infiltration profiles across HCC tumor and non-tumor liver samples. **(b)** Comparison of immune cell infiltration levels between tumor and non-tumor tissues, showing significant depletion of multiple immune cell populations in tumors. **(c)** Correlation matrix among infiltrating immune cell populations, showing strong positive associations among depleted immune cell subsets. **(d)** Correlation analysis between key gene expression and immune cell infiltration levels, showing inverse associations of SNX27 and PEA15 with multiple immune cell populations. Statistical significance was defined as follows: $P < 0.05$, *; $P < 0.01$, **; and $P < 0.001$, ***.

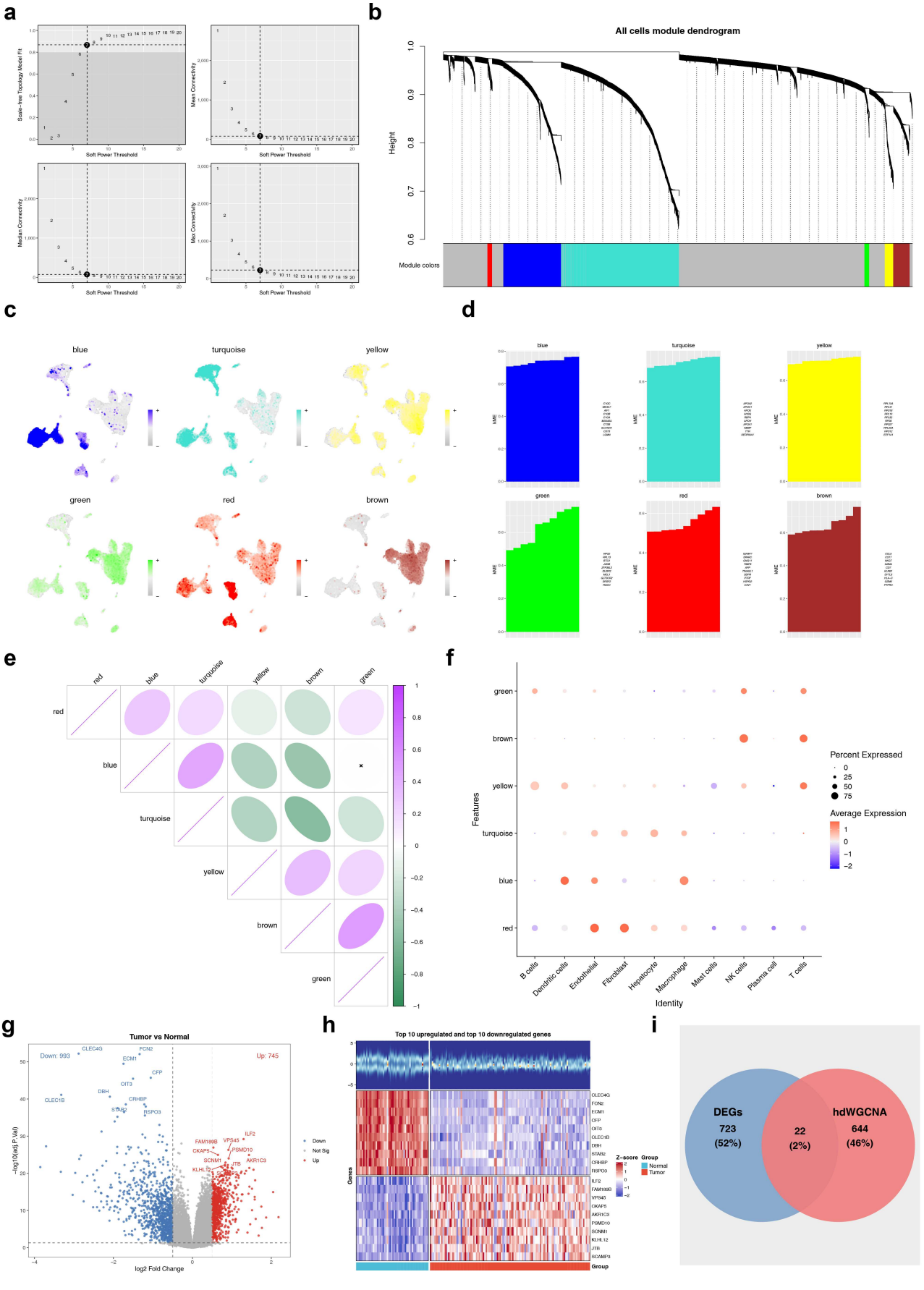
Fig. 6. Macrophages exhibited metabolic reprogramming with dynamic key gene expression along differentiation trajectories. **(a)** Pathway enrichment analysis across major cell types, highlighting distinct biological programs in hepatocytes and macrophages. **(b)** Single-cell metabolic activity landscape comparing tumor and non-tumor samples across cell types. **(c)** Differentially activated metabolic pathways in tumor macrophages. **(d)** Transcription factor activity inference across cell types, showing elevated STAT6, KLF4, RFX5, FLI1, ESR2, and CDX2 activity in macrophages. **(e)** UMAP visualization of macrophage subtypes, including Macro_MARCO, Macro_BAG3, Macro_VCAN, Macro_CXCL9, Macro_MMP9, and Macro_TOP2A. **(f)** Pseudotime trajectory of macrophage differentiation showing a branching structure from early to terminal states. **(g)** Dynamic expression of PEA15 and SNX27 along macrophage pseudotime, showing relatively stable PEA15 expression and gradual upregulation of SNX27.

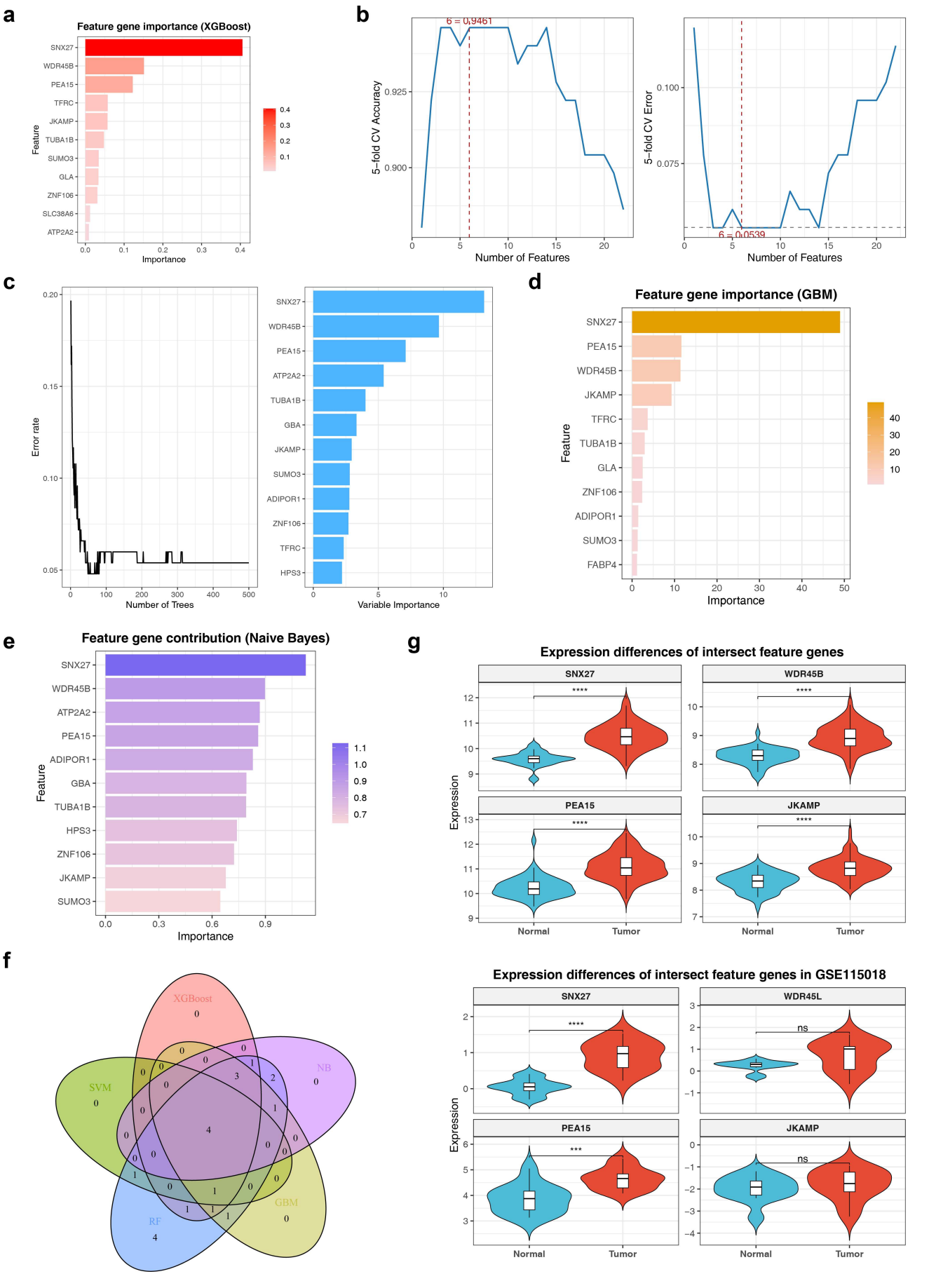
Fig. 7. Trabectedin formed stable complexes with both key gene-encoded proteins. **(a)** Top-ranked candidate compounds predicted by GraphBAN for SNX27 and PEA15 based on combined drug-target interaction scores. **(b)** Molecular docking pose of SNX27 with trabectedin. **(c)** Molecular docking pose of SNX27 with farnesyl pyrophosphate. **(d)** Molecular docking pose of PEA15 with trabectedin. **(e)** Molecular docking pose of PEA15 with farnesyl pyrophosphate. **(f)** Root mean square deviation (RMSD) profiles from 100 ns molecular dynamics simulations of the four protein–ligand complexes. **(g)** Root mean square fluctuation (RMSF) profiles showing residue-level fluctuations during molecular

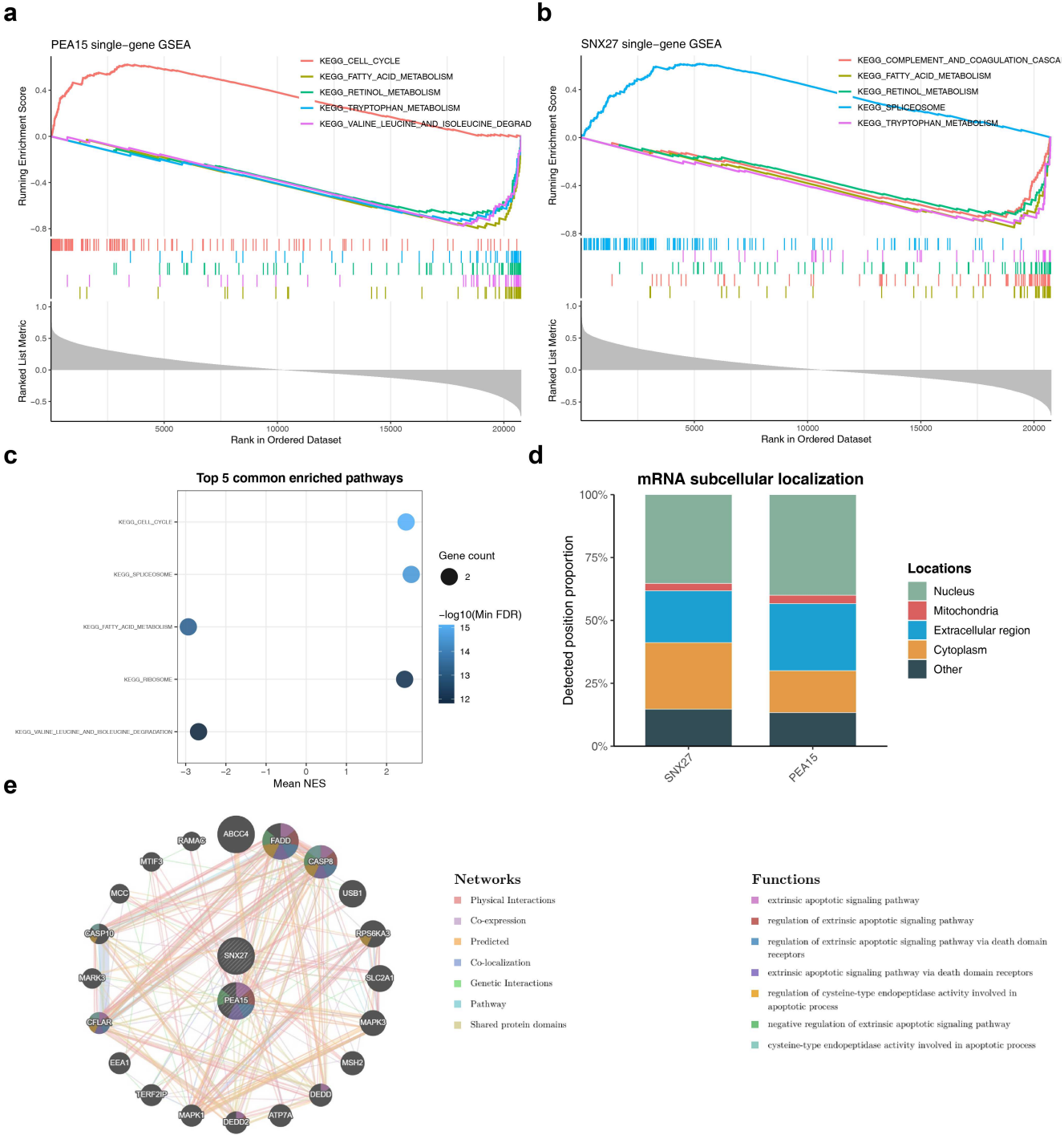
dynamics simulations. **(h)** Total energy trajectories of the simulated complexes over 100 ns. **(i)** Hydrogen bond number profiles throughout the simulations.

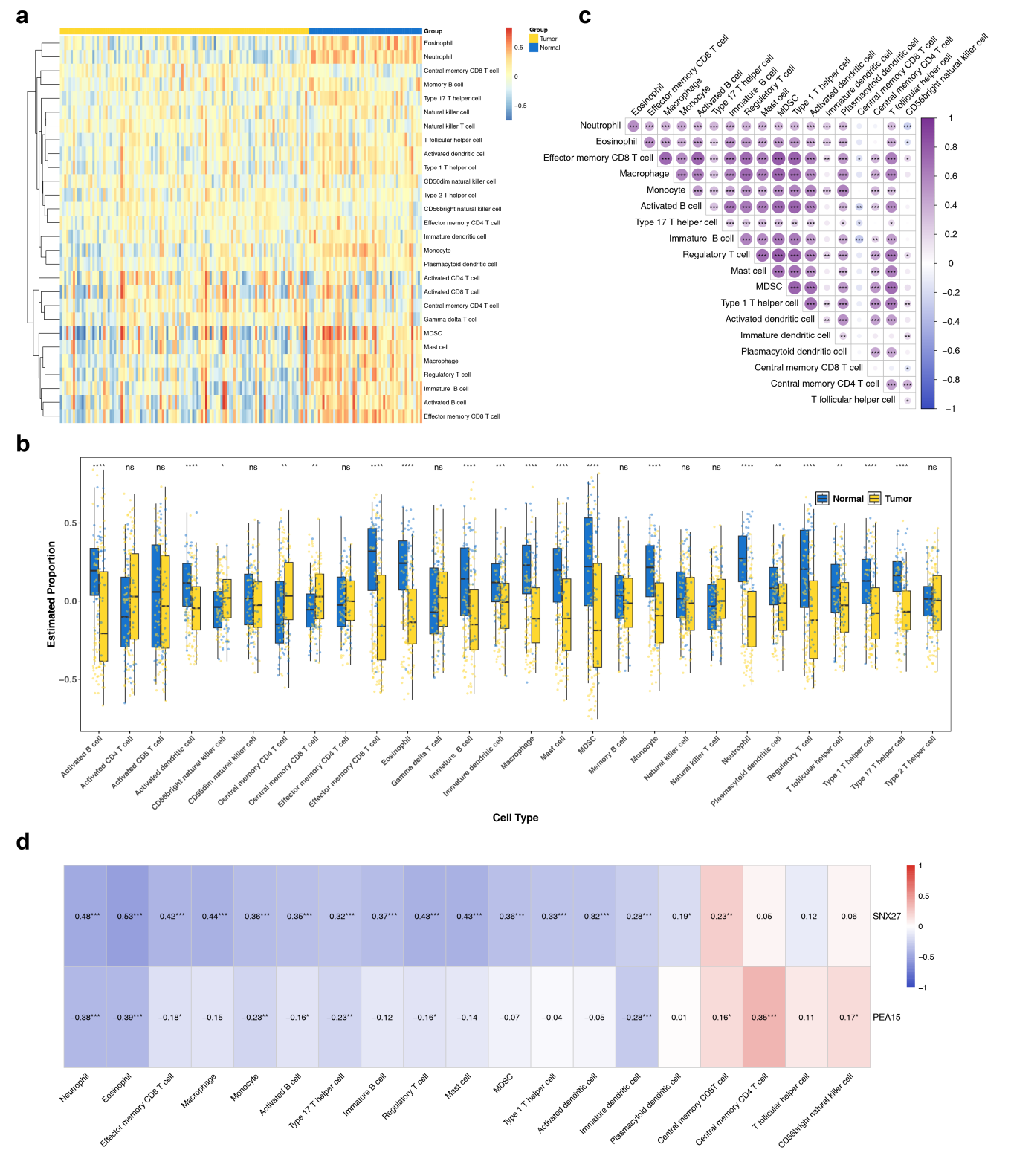
Fig. 8. Expression of there prognostic genes in HCC tissue. **(a)** Expression of components of there prognostic genes in cirrhotic tissues and HCC tissues as assessed by immunohistochemistry. **(b)** Correlation of expression intensities of the three genes in HCC tissues. **(c)** The expression levels of there prognostic genes were also closely related to the degree of differentiation and BLCL stage.**(d)** Kaplan–Meier assessment of the effect of the expression of the there prognostic genes on survival time.

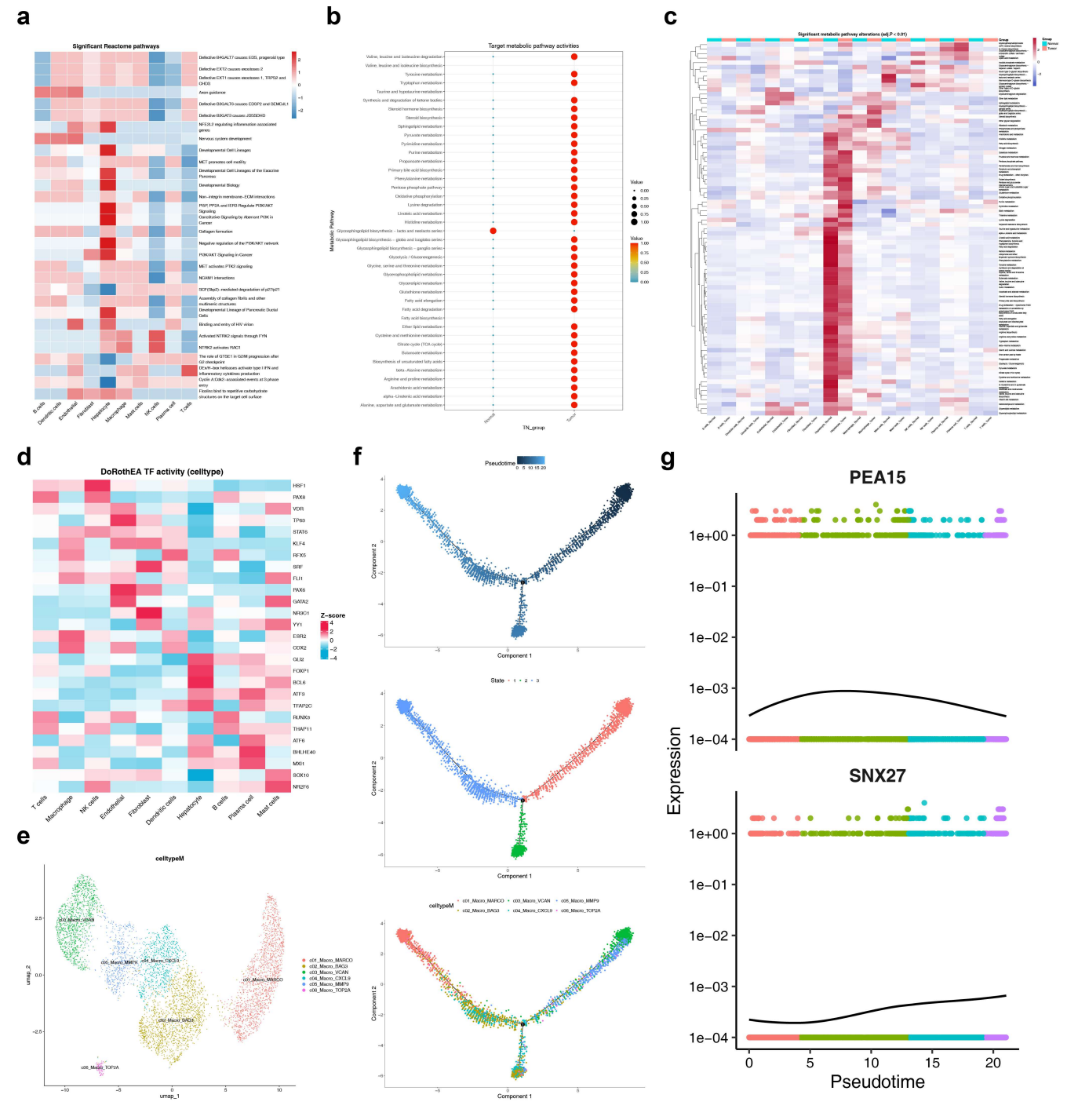

a
celltype
Hepatocyte
Natural Killer cells
T cells
Dendritic cells
Macrophage
Endothelial
Mast cells
Plasma cell
Fibroblast
B cells
umap_1
umap_2
B cells
Dendritic cells
Endothelial
Fibroblast
Hepatocyte
Macrophage
Mast cells
Natural Killer cells
Plasma cell
T cells
b
Features
COL1A2
COL1A1
ACTA2
FCGR2B
PECAM1
VWF
EPCAM
SERPINA1
ALB
CPA3
KIT
LAMP3
CD1C
LILRA4
CD68
LYZ
IGHG2
XBP1
MS4A1
CD79B
CD79A
NKG7
GNLY
CD3G
CD3E
CD3D
T cells
Natural Killer cells
B cells
Plasma cell
Macrophage
Dendritic cells
Mast cells
Hepatocyte
Endothelial
Fibroblast
Identity
Percent Expressed
0
25
50
75
Average Expression
2
1
0
−1
c
NTL ~ Macrophage
NTL ~ Mast cells
NTL ~ Hepatocyte
NTL ~ NK cells
NTL ~ Fibroblast
NTL ~ Plasma cell
NTL ~ Endothelial
NTL ~ T cells
NTL ~ Dendritic cells
PT ~ B cells
NTL ~ B cells
PT ~ Dendritic cells
PT ~ T cells
PT ~ Endothelial
PT ~ Plasma cell
PT ~ Fibroblast
PT ~ NK cells
PT ~ Hepatocyte
PT ~ Mast cells
PT ~ Macrophage
# of Connected Nodes
7
16
20
Overall Score
200
150
100
50
# of Communication Events
1
3
16
d
Number of mCCC event
Sender
Receiver
65
25
58
46
52
43
52
65
45
47
42
23
36
17
36
24
31
28
30
9
29
24
26
13
24
52
18
41
14
3
13
33
13
57
11
1
10
23
9
40
PT ~ Hepatocyte
PT ~ Macrophage
NTL ~ Macrophage
NTL ~ Hepatocyte
NTL ~ Endothelial
NTL ~ Dendritic cells
NTL ~ Mast cells
PT ~ Dendritic cells
PT ~ Endothelial
NTL ~ Fibroblast
PT ~ Mast cells
PT ~ Fibroblast
NTL ~ NK cells
NTL ~ T cells
NTL ~ Plasma cell
PT ~ T cells
PT ~ NK cells
PT ~ Plasma cell
NTL ~ B cells
PT ~ B cells
e
mCCC events
Cluster 1
Cluster 2
Cluster 3
Cluster 4
NTL
PT
Z-score
1.00
0.75
0.50
0.25
0.00
−0.25
−0.50
−0.75
−1.00

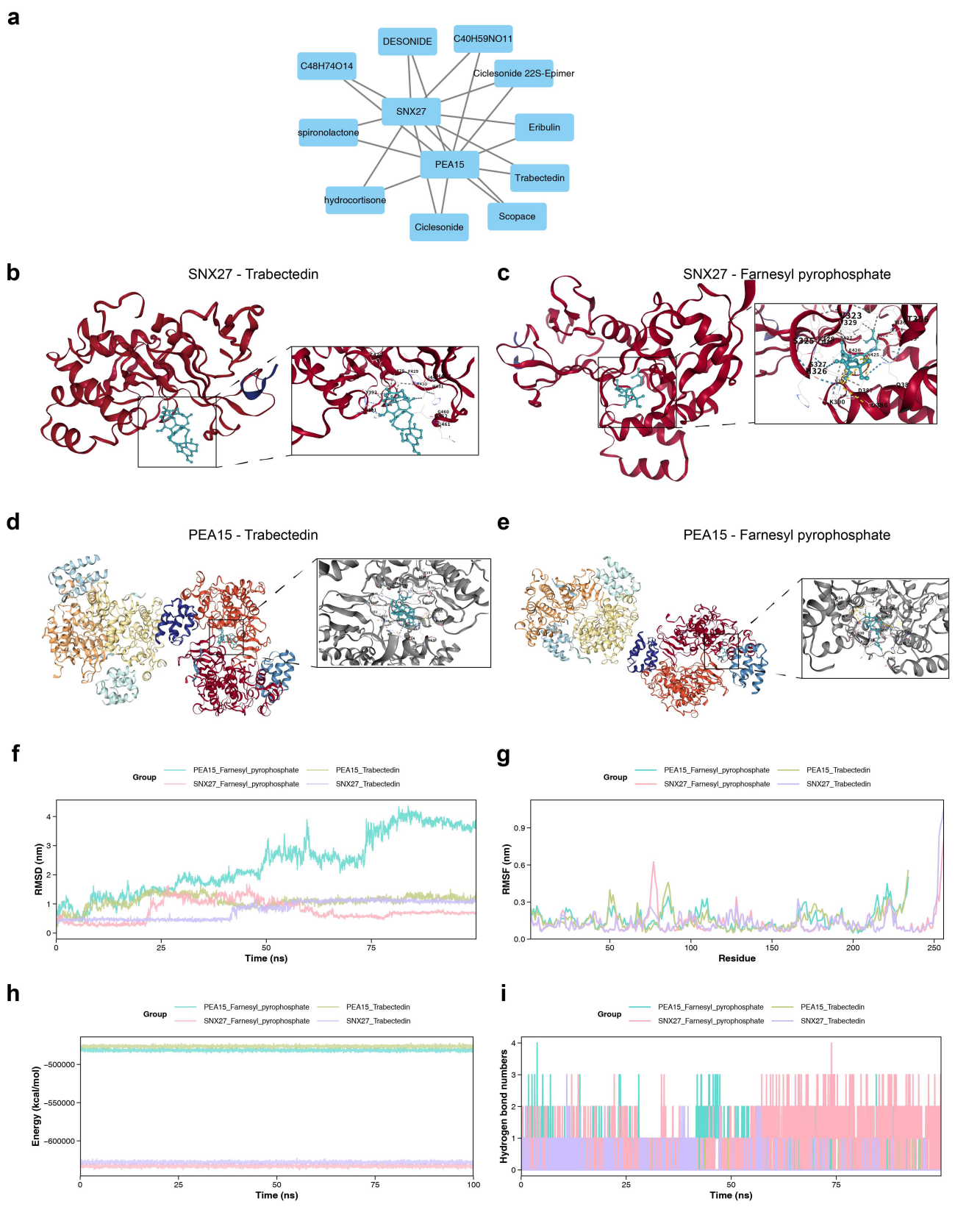

a
Scale-free Topology Model Fit
Mean Connectivity
Median Connectivity
Max Connectivity
Soft Power Threshold
b
All cells module dendrogram
Height
Module colors
c
blue
turquoise
yellow
green
red
brown
d
kME
e
red
blue
turquoise
yellow
brown
green
f
Features
Identity
B cells
Dendritic cells
Endothelial
Fibroblast
Hepatocyte
Macrophage
Mast cells
NK cells
Plasma cell
T cells
Percent Expressed
Average Expression
g
Tumor vs Normal
Down: 993
Up: 745
−log10(adj.P.Val)
log2 Fold Change
Down
Not Sig
Up
h
Top 10 upregulated and top 10 downregulated genes
Genes
Z−score
Group
Normal
Tumor
i
DEGs
723
(52%)
22
(2%)
hdWGCNA
644
(46%)

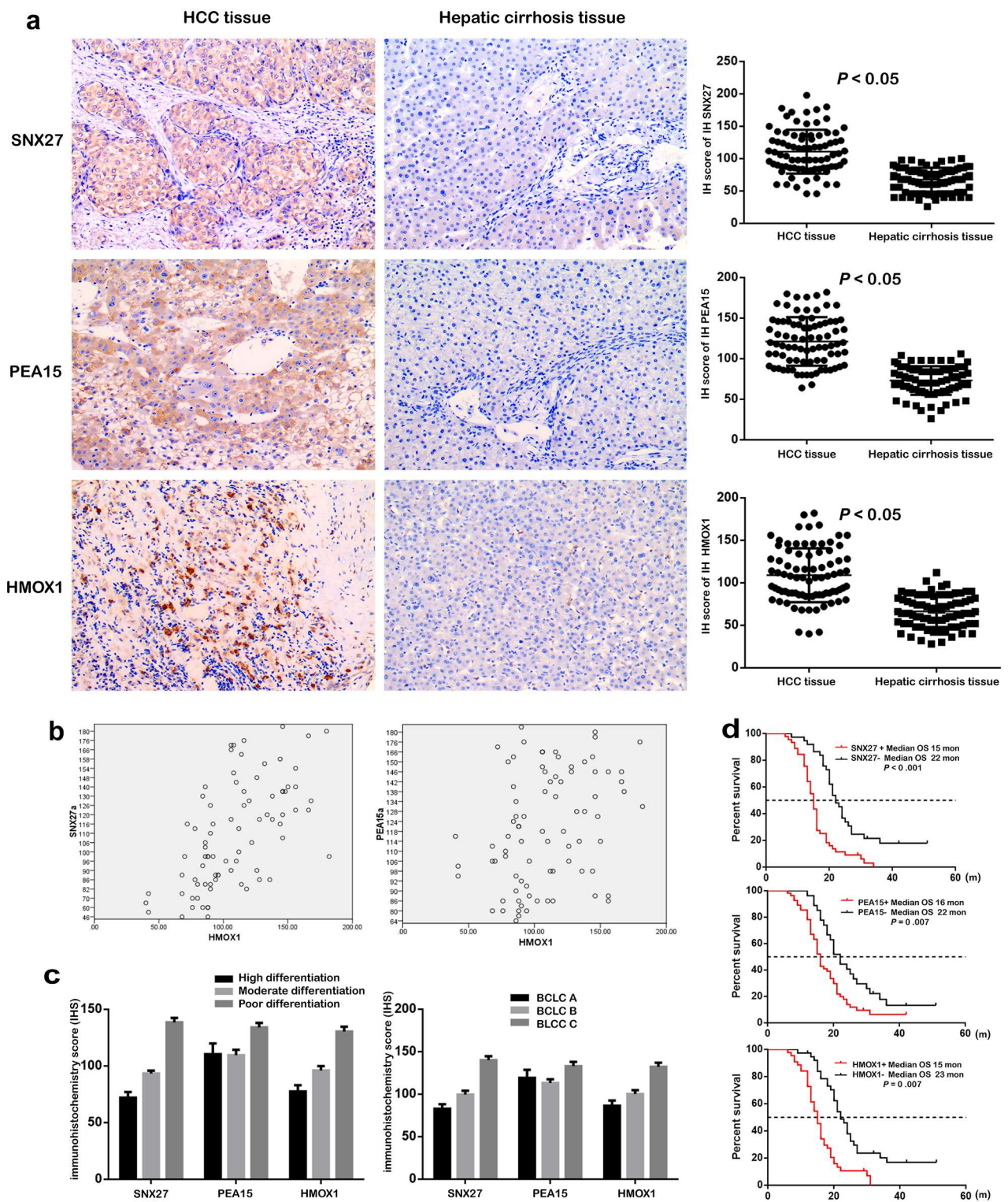

a
Feature gene importance (XGBoost)
SNX27
WDR45B
PEA15
TFRC
JKAMP
TUBA1B
SUMO3
GLA
ZNF106
SLC38A6
ATP2A2
Feature
Importance
b
6 = 0.9461
5−fold CV Accuracy
Number of Features
6 = 0.0539
5−fold CV Error
Number of Features
c
Error rate
Number of Trees
SNX27
WDR45B
PEA15
ATP2A2
TUBA1B
GBA
JKAMP
SUMO3
ADIPOR1
ZNF106
TFRC
HPS3
Variable Importance
d
Feature gene importance (GBM)
SNX27
PEA15
WDR45B
JKAMP
TFRC
TUBA1B
GLA
ZNF106
ADIPOR1
SUMO3
FABP4
Feature
Importance
e
Feature gene contribution (Naive Bayes)
SNX27
WDR45B
ATP2A2
PEA15
ADIPOR1
GBA
TUBA1B
HPS3
ZNF106
JKAMP
SUMO3
Feature
Importance
f
XGBoost
SVM
NB
RF
GBM
g
Expression differences of intersect feature genes
SNX27
WDR45B
PEA15
JKAMP
Expression
Normal
Tumor
Expression differences of intersect feature genes in GSE115018
SNX27
WDR45L
PEA15
JKAMP
Expression
Normal
Tumor


a
PEA15 single−gene GSEA
KEGG_CELL_CYCLE
KEGG_FATTY_ACID_METABOLISM
KEGG_RETINOL_METABOLISM
KEGG_TRYPTOPHAN_METABOLISM
KEGG_VALINE_LEUCINE_AND_ISOLEUCINE_DEGRAD
Running Enrichment Score
Ranked List Metric
Rank in Ordered Dataset
b
SNX27 single−gene GSEA
KEGG_COMPLEMENT_AND_COAGULATION_CASCA
KEGG_FATTY_ACID_METABOLISM
KEGG_RETINOL_METABOLISM
KEGG_SPLICEOSOME
KEGG_TRYPTOPHAN_METABOLISM
Running Enrichment Score
Ranked List Metric
Rank in Ordered Dataset
c
Top 5 common enriched pathways
KEGG_CELL_CYCLE
KEGG_SPLICEOSOME
KEGG_FATTY_ACID_METABOLISM
KEGG_RIBOSOME
KEGG_VALINE_LEUCINE_AND_ISOLEUCINE_DEGRADATION
Mean NES
Gene count
−log10(Min FDR)
d
mRNA subcellular localization
Detected position proportion
SNX27
PEA15
Locations
Nucleus
Mitochondria
Extracellular region
Cytoplasm
Other
e
ABCC4
FADD
RAMA6
MTIF3
CASP8
MCC
USB1
CASP10
RPS6KA3
SNX27
MARK3
SLC2A1
PEA15
CFLAR
MAPK3
EEA1
MSH2
TERF2IP
DEDD
MAPK1
DEDD2
ATP7A
Networks
Physical Interactions
Co-expression
Predicted
Co-localization
Genetic Interactions
Pathway
Shared protein domains
Functions
extrinsic apoptotic signaling pathway
regulation of extrinsic apoptotic signaling pathway
regulation of extrinsic apoptotic signaling pathway via death domain receptors
extrinsic apoptotic signaling pathway via death domain receptors
regulation of cysteine-type endopeptidase activity involved in apoptotic process
negative regulation of extrinsic apoptotic signaling pathway
cysteine-type endopeptidase activity involved in apoptotic process


a
Group
Tumor
Normal
Eosinophil
Neutrophil
Central memory CD8 T cell
Memory B cell
Type 17 T helper cell
Natural killer cell
Natural killer T cell
T follicular helper cell
Activated dendritic cell
Type 1 T helper cell
CD56dim natural killer cell
Type 2 T helper cell
CD56bright natural killer cell
Effector memory CD4 T cell
Immature dendritic cell
Monocyte
Plasmacytoid dendritic cell
Activated CD4 T cell
Activated CD8 T cell
Central memory CD4 T cell
Gamma delta T cell
MDSC
Mast cell
Macrophage
Regulatory T cell
Immature B cell
Activated B cell
Effector memory CD8 T cell
c
Eosinophil
Effector memory CD8 T cell
Macrophage
Monocyte
Activated B cell
Type 17 T helper cell
Immature B cell
Regulatory T cell
Mast cell
MDSC
Type 1 T helper cell
Activated dendritic cell
Immature dendritic cell
Plasmacytoid dendritic cell
Central memory CD8 T cell
Central memory CD4 T cell
T follicular helper cell
CD56bright natural killer cell
Neutrophil
Eosinophil
Effector memory CD8 T cell
Macrophage
Monocyte
Activated B cell
Type 17 T helper cell
Immature B cell
Regulatory T cell
Mast cell
MDSC
Type 1 T helper cell
Activated dendritic cell
Immature dendritic cell
Plasmacytoid dendritic cell
Central memory CD8 T cell
Central memory CD4 T cell
T follicular helper cell
b
Normal
Tumor
Estimated Proportion
Cell Type
Activated B cell
Activated CD4 T cell
Activated CD8 T cell
Activated dendritic cell
CD56bright natural killer cell
CD56dim natural killer cell
Central memory CD4 T cell
Central memory CD8 T cell
Effector memory CD4 T cell
Effector memory CD8 T cell
Eosinophil
Gamma delta T cell
Immature B cell
Immature dendritic cell
Macrophage
Mast cell
MDSC
Memory B cell
Monocyte
Natural killer cell
Natural killer T cell
Neutrophil
Plasmacytoid dendritic cell
Regulatory T cell
T follicular helper cell
Type 1 T helper cell
Type 17 T helper cell
Type 2 T helper cell
d
SNX27
PEA15
Neutrophil
Eosinophil
Effector memory CD8 T cell
Macrophage
Monocyte
Activated B cell
Type 17 T helper cell
Immature B cell
Regulatory T cell
Mast cell
MDSC
Type 1 T helper cell
Activated dendritic cell
Immature dendritic cell
Plasmacytoid dendritic cell
Central memory CD8T cell
Central memory CD4 T cell
T follicular helper cell
CD56bright natural killer cell


a
Significant Reactome pathways
Defective B4GALT7 causes EDS, progeroid type
Defective EXT2 causes exostoses 2
Defective EXT1 causes exostoses 1, TRPS2 and CHDS
Axon guidance
Defective B3GALT6 causes EDSSPD and SEMDJL1
Defective B3GAT3 causes JDSSDHD
NFE2L2 regulating inflammation associated genes
Nervous system development
Developmental Cell Lineages
MET promotes cell motility
Developmental Cell Lineages of the Exocrine Pancreas
Developmental Biology
Non-integrin membrane-ECM interactions
PI3/T, PP2A and IER3 Regulate PI3K/AKT Signaling
Constitutive Signaling by Aberrant PI3K in Cancer
Collagen formation
Negative regulation of the PI3K/AKT network
PI3K/AKT Signaling in Cancer
MET activates PTK2 signaling
NCAM1 interactions
SCF(Skp2)-mediated degradation of p27/p21
Assembly of collagen fibrils and other multimeric structures
Developmental Lineage of Pancreatic Ductal Cells
Binding and entry of HIV virion
Activated NTRK2 signals through FYN
NTRK2 activates RAC1
The role of GITR1 in G2/M progression after G2 checkpoint
DExH-box helicases activate type I IFN and inflammatory cytokines production
Cyclin A:Cdk2-associated events at S phase entry
Fixelins bind to repetitive carbohydrate structures on the target cell surface
B cells
Dendritic cells
Endothelial
Fibroblast
Hepatocyte
Macrophage
Mast cells
NK cells
Plasma cell
T cells
b
Target metabolic pathway activities
Valine, leucine and isoleucine degradation
Valine, leucine and isoleucine biosynthesis
Tyrosine metabolism
Tryptophan metabolism
Taurine and hypotaurine metabolism
Synthesis and degradation of ketone bodies
Steroid hormone biosynthesis
Steroid biosynthesis
Sphingolipid metabolism
Pyruvate metabolism
Pyrimidine metabolism
Purine metabolism
Propanoate metabolism
Primary bile acid biosynthesis
Phenylalanine metabolism
Pentose phosphate pathway
Oxidative phosphorylation
Lysine degradation
Linoleic acid metabolism
Histidine metabolism
Glycosphingolipid biosynthesis – lacto and neolacto series
Glycosphingolipid biosynthesis – globo and isoglobo series
Glycosphingolipid biosynthesis – ganglio series
Glycolysis / Gluconeogenesis
Glycine, serine and threonine metabolism
Glycerophospholipid metabolism
Glycerolipid metabolism
Glutathione metabolism
Fatty acid elongation
Fatty acid degradation
Fatty acid biosynthesis
Ether lipid metabolism
Cysteine and methionine metabolism
Citrate cycle (TCA cycle)
Butanoate metabolism
Biosynthesis of unsaturated fatty acids
beta-Alanine metabolism
Arginine and proline metabolism
Arachidonic acid metabolism
alpha-Linolenic acid metabolism
Alanine, aspartate and glutamate metabolism
Metabolic Pathway
Normal
Tumor
TN_group
Value
c
Significant metabolic pathway alterations (adj.P < 0.01)
Group
Normal
Tumor
d
DoRothEA TF activity (celltype)
HSF1
PAX8
VDR
TP63
STAT6
KLF4
RFX5
SRF
FLI1
PAX6
GATA2
NR3C1
YY1
ESR2
CDX2
GLI2
FOXP1
BCL6
ATF3
TFAP2C
RUNX3
THAP11
ATF6
BHLHE40
MXI1
SOX10
NR2F6
Z-score
T cells
Macrophage
NK cells
Endothelial
Fibroblast
Dendritic cells
Hepatocyte
B cells
Plasma cell
Mast cells
e
celltypeM
c01_Macro_MARCO
c02_Macro_SAG3
c03_Macro_VCAN
c04_Macro_CXCL9
c05_Macro_MMP9
c06_Macro_TOP2A
umap_1
umap_2
f
Pseudotime
Component 1
Component 2
State
celltypeM
g
PEA15
SNX27
Expression
Pseudotime


a
DESONIDE
C40H59NO11
C48H74O14
Ciclesonide 22S-Epimer
SNX27
spironolactone
Eribulin
PEA15
Trabectedin
hydrocortisone
Scopace
Ciclesonide
b
SNX27 - Trabectedin
c
SNX27 - Farnesyl pyrophosphate
d
PEA15 - Trabectedin
e
PEA15 - Farnesyl pyrophosphate
f
Group
PEA15_Farnesyl_pyrophosphate
SNX27_Farnesyl_pyrophosphate
PEA15_Trabectedin
SNX27_Trabectedin
RMSD (nm)
Time (ns)
g
Group
PEA15_Farnesyl_pyrophosphate
SNX27_Farnesyl_pyrophosphate
PEA15_Trabectedin
SNX27_Trabectedin
RMSF (nm)
Residue
h
Group
PEA15_Farnesyl_pyrophosphate
SNX27_Farnesyl_pyrophosphate
PEA15_Trabectedin
SNX27_Trabectedin
Energy (kcal/mol)
Time (ns)
i
Group
PEA15_Farnesyl_pyrophosphate
SNX27_Farnesyl_pyrophosphate
PEA15_Trabectedin
SNX27_Trabectedin
Hydrogen bond numbers
Time (ns)


a
HCC tissue
Hepatic cirrhosis tissue
SNX27
PEA15
HMOX1
P < 0.05
IH score of IH SNX27
IH score of IH PEA15
IH score of IH HMOX1
HCC tissue
Hepatic cirrhosis tissue
b
SNX27a
PEA15a
HMOX1
c
High differentiation
Moderate differentiation
Poor differentiation
BCLC A
BCLC B
BLCC C
immunohistochemistry score (IHS)
SNX27
PEA15
HMOX1
d
SNX27 + Median OS 15 mon
SNX27- Median OS 22 mon
P < 0 .001
PEA15+ Median OS 16 mon
PEA15- Median OS 22 mon
P = 0 .007
HMOX1+ Median OS 15 mon
HMOX1- Median OS 23 mon
P = 0 .007
Percent survival
(m)

Supplementary Files

This is a list of supplementary files associated with this preprint. Click to download.

- Table1.docx
- Table2.docx
- SupplementaryMaterials.zip